1   **W-band S/Z Relationships for Rimed Snow Particles: Observational Evidence from**

2   **Combined Airborne and Ground-based Observations**

4   Shelby Fuller [1], Sam Marlow [1], Samuel Haimov [1], Matthew Burkhart [1], Kevin Shaffer [1], Austin

5   Morgan [1], and Jefferson R. Snider [1,2]

7   [1] Department of Atmospheric Science, University of Wyoming, Laramie, WY, USA
8
9
10
11   [2] Corresponding Author, jsnider@uwyo.edu

13   **Abstract**

14   Values of undercatch-corrected liquid-equivalent snowfall rate (S) at a ground site and

15   microwave reflectivity (Z) retrieved using an airborne W-band radar were acquired during

16   overflights. The temperature at the ground site was between -6 and -15 $^{\circ}$C. At flight level, within

17   clouds containing ice and supercooled liquid water, the temperature was approximately 7 $^{\circ}$C

18   colder. Additionally, airborne measurements of snow particle imagery were acquired. The

19   images demonstrate that most of the snow particles were rimed, at least a flight level. A

20   relatively small set of S/Z pairs (4) are available from the overflights. Important distinctions

21   between these measurements and those of Pokharel and Vali (2011), who also reported W-band

22   S/Z pairs for rimed snow particles, are 1) the fewer number of S/Z pairs, 2) the method used to

23   acquire S, and 3) the altitude, relative to ground, of the Z retrievals. This analysis indicates that

24   the S/Z relationship reported in Pokharel and Vali (2011) yields an S, in scenarios with snowfall

25   produced by riming, that is substantially larger than that derived using an S/Z relationship

26   developed for unrimed snow particles.

1 - Introduction

Improvement of methods used to measure snowfall and rainfall are an ongoing focus of meteorological research. The various methods are ground-based instruments that evaluate the mass of precipitation that falls into or onto a collector (precipitation gauges) (Brock and Richardson 2001), ground-based radars (Wilson and Brandes 1979), and airborne and space-borne radars (Matrosov 2007; Kulie and Bennartz 2009; Geerts et al. 2010; Skofronick-Jackson et al. 2017). An objective of these approaches, whether used to make observations independent of other methods (e.g., Kulie and Bennartz 2009), or as a component of multiple observations (e.g., Cocks et al. 2016), is estimation of precipitation rate and accumulation.

Many studies have investigated using radar for evaluating rainfall (for a review see Wilson and Brandes 1979). There are two approaches. The first is research, both observational and computational, that probes the relationship between rainfall rate (R) and radar-measured values of range-corrected backscattered microwave power. The latter is commonly reported as an equivalent radar reflectivity factor (Z_e). The second is operational in the sense that precipitation gauges are used to calibrate measurements acquired using weather surveillance radars. Complications associated with converting Z_e to R, or converting a radar reflectivity factor[1] (Z) to R, can be grouped in four categories: 1) Inaccuracy in quantification of Z, 2) variation of the R/Z relationship stemming from precipitation processes (e.g., coalescence and break up), 3) difference between the volume of a radar range gate versus the much smaller volume of atmosphere sampled as precipitation falls to a gauge, and 4) vertical displacement between a radar range gate and a calibrating gauge, especially at far ranges.

---

[1] Radars are calibrated to report Z_e (Smith 1984). Herein, radar reflectivities are reported as Z = Z_e and as dBZ = $10\log_{10}(Z_e)$.

49   For situations with snowfall, methods employing either gauge or radar are associated

50   with complications beyond that incurred in rainfall (Matrosov 2007; Martinaitis et al. 2015;

51   Cocks et al. 2016). Problems associated with gauge measurements are wind-induced snow

52   particle undercatch, gauge capping, delayed registration, and blowing snow aliasing as snowfall.

53   Moreover, in a situation with snow particles most abundant within a radar range gate, compared

54   to rain drops, and where a measurement of Z is used to infer R via a R/Z relationship, the

55   resultant precipitation rate will likely be inaccurate. This is because hydrometeor shape, density,

56   and dielectric properties are all variable for snow particles while relatively invariant for rain

57   drops. Additionally, a snow particle's terminal fall speed varies with size (as is the case for

58   drops) and with particle shape and particle density. Going forward, we refer to the latter two

59   properties as shape and density.

60   The goals of this paper are as follows: 1) to describe measurements of undercatch-

61   corrected liquid-equivalent snowfall rate (S, mm h^{-1}) and how these were paired with W-band

62   measurements of reflectivity (Z, mm^6 m^{-3}) ; 2) to contrast the S/Z pairs against S/Z relationships

63   commonly applied in radar retrievals of S; and 3) to investigate why the S/Z pairs deviate from

64   predictions of some S/Z relationships.

65   In calculations of paired values of S and Z, density is an important parameter. Density is

66   commonly estimated using empirical data (e.g., Pokharel and Vali 2011, [PV11]). For graupel, a

67   snow particle that grows via collection of supercooled cloud droplets in a process commonly

68   referred to as riming, paired observations of particle mass and particle size have been used to

69   estimate density. There is considerable uncertainty in this approach. Based on data collected at

70   two northwestern US surface sites (Zikmunda and Vali 1972; Locatelli and Hobbs 1974), density

71   values differ by at least a factor of two at particle sizes smaller than 2000 μm (PV11; their Fig.

72 4). Given that the density of rime ice varies with droplet impact speed, droplet size, and

73 temperature (Macklin 1962), it is not surprising that the density-size relationships analyzed by

74 PV11 are so varied.

75   The following introductory paragraphs overview W-band S/Z relationships being applied

76 in instances of snowfall where mass is acquired by vapor deposition (crystal), by collection of

77 crystals (aggregate), and by riming (rimed crystal and graupel). Henceforth, the latter two snow

78 particle types are collectively referred to as rimed snow particles.

79   In a computational study, Hiley et al. (2011) considered a variety of snow particle types

80 (column, plate, bullet rosette, sector plate, dendrite, and aggregate), employed a parameterized

81 ice particle size distribution (PSD) function (Field et al. 2005), accounted for a range of

82 temperature (-5 to -15 $^{\circ}$C) via the Field et al. parameterization, and developed a range of S/Z

83 relationships for snow particles. Except for the aggregates, the modeled particle types were

84 vapor-grown crystals. Hiley et al.'s upper- and lower-limit relationships are S = 0.21·$Z^{0.77}$ and S

85 = 0.024·$Z^{0.91}$. Matrosov (2007) developed an S/Z relationship for aggregates. In that work,

86 parameterized PSDs from Braham (1990) were employed, and a range of particle aspect ratios

87 were factored into the calculations. For aggregates, the S/Z relationship is S = 0.056·$Z^{1.25}$

88 (Matrosov 2007). It should be noted that Hiley et al. (2011) and Matrosov (2007) employed

89 similar, but not identical, computational methods. Kulie and Bennartz (2009) developed an S/Z

90 relationship for what they referred to as a "snow particle" type. The wavelength-dependent

91 density derived by Surussavadee and Staelin (2007) (200 kg m^{-3} at λ = 3.2 mm) was adopted, the

92 snow particles were modeled as spheres, and the Field et al. parameterization was applied. The

93 S/Z relationship developed for this particle type is S = 0.52·$Z^{0.83}$ (Surussavadee and Staelin 2007;

94 Kulie and Bennartz 2009; henceforth SSKB). Variance in the calculations discussed in this

95   paragraph originate from changes in density, shape, fall speed, PSD, and particle size as these

96   changes are propagated through the cloud-microphysical and microwave-scattering calculations.

97   In a hybrid approach (computational and an analysis of airborne observations), PV11

98   concluded that most of the snow particles they imaged were rimed snow particles. Values of S

99   were calculated using a density-size function (ρ_1, discussed below), a fall speed-size function, a

100   measured PSD and measured particle images, and a determination of particle volumes. It was

101   assumed that a prolate spheroid approximated particle shape and this was the basis for

102   determining a particle's sphere-equivalent volume and the particle's sphere-equivalent size. The

103   sphere-equivalent size was applied in the two functions. Values of Z were calculated using a

104   measured PSD, sphere-equivalent sizes, the ρ_1 function, and Mie Theory. PV11 presented

105   calculations of Z, obtained using two density-size relationships (their Eqs. 1 and 2) and compared

106   their calculated reflectivities to measurements of Z from a W-band radar. That led to their

107   conclusion that "...the lower density assumption…yielded closer correspondence to observed

108   reflectivities." Their recommendation for S as a function of measured Z - hereafter the $S(\rho_1)/Z$

109   best-fit line - is $S = 0.39 \cdot Z^{0.58}$. Values of Z that were paired with the calculated values of S (i.e.,

110   the S/Z pairs from PV11 that we present in Sect. 4), and that were used to determine the $S(\rho_1)/Z$

111   best-fit line, came from the WCR. In addition to variance in their values of S, coming from a

112   dependence on density, PV11 state that a value of S derived via their best-fit line is uncertain by

113   a factor-of-ten. That uncertainty is evident in the variance of S/Z data pairs about the $S(\rho_1)/Z$ line

114   in Fig. 11 of PV11. Those investigators, and Geerts et al. (2010), attributed the variance to use of

115   two-dimensional snow particle images in calculations of S and to actual variations of density,

116   shape, and particle size not accounted for in the calculations.

117   Also relevant are S/Z relationships reported by Falconi et al. (2018; their Table 2). These

118   were developed using measurements from a video disdrometer, weighing precipitation gauge,

119   microwave radiometer, and a vertically-pointing W-band radar. All these systems were operated

120   at the ground. The data set was stratified into intervals of lightly-rimed, moderately-rimed, and

121   heavily-rimed snow. A proxy for snow particle riming - radiometer measurements of liquid water

122   path – was the basis for the stratifications (von Lerber et al. 2017). The S/Z relationships are $S =$

123    $0.10 \cdot Z^{1.0}$ (lightly-rimed), $S = 0.079 \cdot Z^{1.3}$ (moderately-rimed), and $S = 0.060 \cdot Z^{1.4}$ (heavily-rimed).

124   Our focus is on surface measurements of S and on pairing of those measurements with

125   airborne measurements of Z. We also analyze airborne measurements of snow particle imagery.

126   The latter demonstrates that the particles observed at flight level were rimed. These

127   measurements are the basis for our assertion that our data set is relevant to ongoing

128   investigations of using Z to evaluate S in situations where precipitation is produced by riming.

129   Section 2 describes the setting of our study, the instruments we deployed, and recordings

130   we obtained using two data acquisition systems. One of the data systems was operated at a

131   ground site and the other on an aircraft. Section 3 is an analysis of the recordings; this section

132   also considers recordings from two additional, but ancillary, ground sites. Our findings are

133   discussed in Sect. 4 and summarized in Sect. 5. An Appendix (Sect. 6) explains how we

134   averaged recordings of near-surface W-band reflectivities and surface-based recordings of

135   snowfall.

2 - Site, Aircraft, and Instruments

2.1 - Site

136

137

138   Analyzed herein are aircraft and ground data from 14/15 December 2016 and from 3

139   January 2017. The ground data were acquired in a forest/prairie ecotone on the eastern slope of

140   the Medicine Bow Mountains in southeast Wyoming (Figs. 1a-b). No ground-based observers

141   were deployed during the two snowfall events analyzed.

142   At one of three ground sites (HP in Figs. 1a-b) a hotplate precipitation gauge (Rasmussen

143   et al. 2011; Zelasko et al. 2018), a GPS receiver, and a data acquisition system were deployed.

144   Once per second, the data system ingested a hotplate-generated data string, combined that with

145   time-of-day from the GPS receiver [Coordinated Universal Time (UTC)], and recorded the

146   merged hotplate/UTC data string. The absolute accuracy of the time stamp is no worse than 2 s.

147   Overflights of the hotplate were done by the University of Wyoming King Air (WKA) on

148   14/15 December 2016 and on 3 January 2017. The flights were conducted in preparation for the

149   SNOWIE field project (Tessendorf et al. 2019) and were flown from the Laramie, WY Airport

150   (LA in Fig. 1a). Data acquisition on the WKA was also synchronized with UTC, but with much

151   better accuracy than at the hotplate.

152

153   Measurements of horizontal wind (speed and direction), temperature, relative humidity,

154   and pressure from the US-GLE AmeriFlux tower (AF in Figs. 1a-b) are also components the

155   analysis. The AmeriFlux data were provided to us as 30-minute averages (AmeriFlux 2021;

156   Marlow et al. 2023).

157
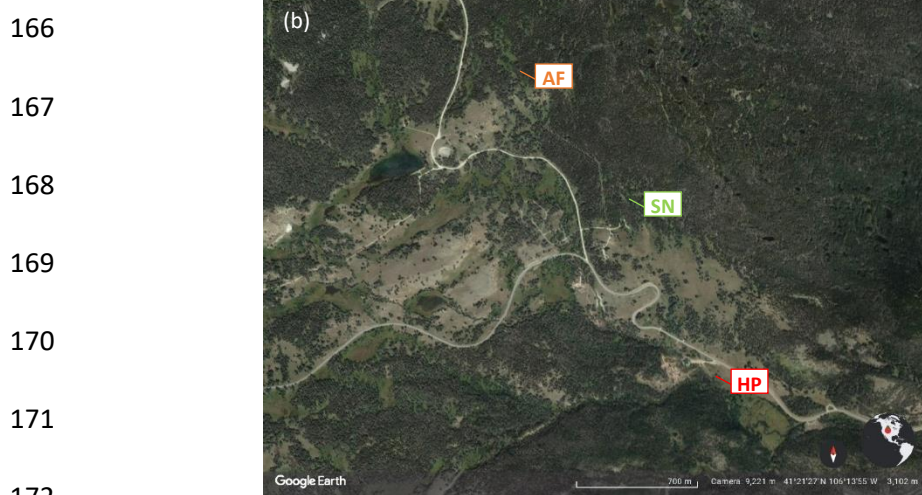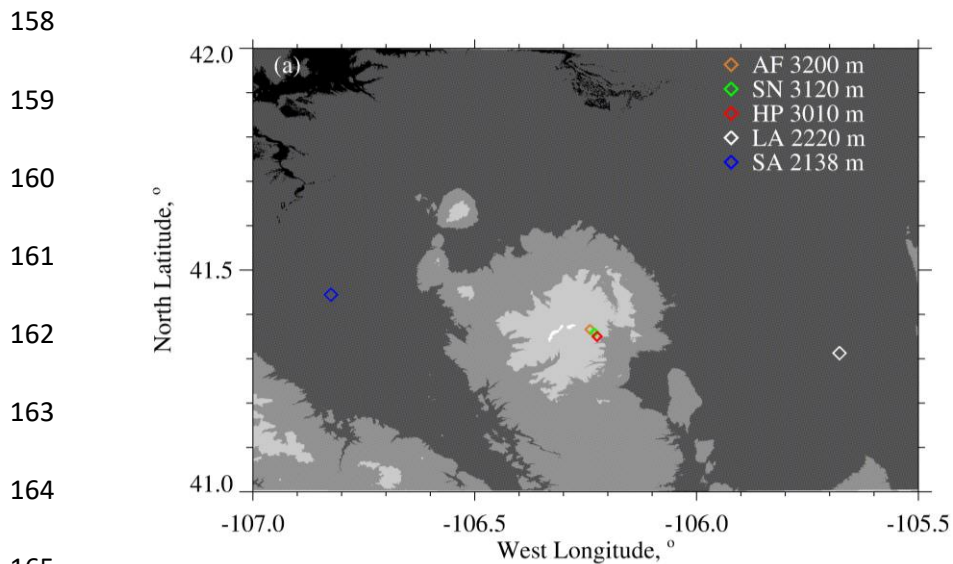
Figure 1 – (a) Southeast Wyoming, airport at Saratoga, WY (SA), airport at Laramie, WY (LA),

and the ground sites: AF = US-GLE AmeriFlux tower, SN = Brooklyn Lake SNOTEL, and HP =

hotplate. Altitudes of the airports and ground sites are in the legend. Altitude thresholds for the

digital elevation map are 1500, 2000, 2500, 3000, and 3500 meters. (b) Close up of the AF, SN,

and HP ground sites (from © Google Earth).

2.2 - University of Wyoming King Air (WKA)

The following WKA measurements were analyzed: aircraft position, temperature, snow particle imagery, and three moments of the cloud droplet size distribution function. A Cloud Droplet Probe (CDP; Faber et al. 2018) was the basis for the droplet size distribution measurements and the derived moments. The latter are droplet concentration (N), cloud liquid water content (LWC), and mean droplet diameter (<D>). Snow particle imagery was obtained using a precipitation particle imaging probe (2DP; Korolev et al. 2011) and a cloud particle imaging probe (2DS; Lawson et al. 2006). These acquired two-dimensional images of particles between 200 to 6400 μm (2DP) and between 10 to 1280 μm (2DS).

2.3 – The W-band Wyoming Cloud Radar (WCR)

Retrievals from the up-looking and down-looking antennas of the WCR, operated on the WKA, were also analyzed. For this we used Level 2 WCR data[2] with reflectivities recorded as $dBZ = 10 \cdot \log_{10}(Z)$. The reflectivities were converted from dBZ to Z prior to processing. Additionally, values of the vertical-component Doppler velocity retrieved from below the WKA using the WCR's down-looking antenna were analyzed. The Doppler velocities were corrected for aircraft motion as described in Haimov and Rodi (2013). We use V_D to symbolize the corrected vertical-component Doppler velocity and adopt the convention that $V_D > 0$ indicates upward hydrometeor motion.

---

[2] http://flights.uwyo.edu/uwka/wcr/projects/snowie17/PROCESSED_DATA/

199   The Level 2 WCR sampling was different on the two flight days and this difference is

200 shown in Table 1. Ground-based calibrations of the WCR's up-looking antenna and correlations

201 between in-flight retrievals acquired using the WCR's up-looking and down-looking antennas

202 were used to estimate the precision and absolute accuracy of the WCR-derived values of dBZ.

203 These are $\pm$ 1.0 dBZ and $\pm$ 2.5 dBZ, respectively (PV11).

204

205   Table 1 – Level 2 WCR sampling and the WKA overflight time

206

Date	Level 2 WCR Vertical Sampling, m	Level 2 WCR Along-track Sampling, s	Overflight Time, UTC
14/15 December 2016	23	0.23	00:00:38 (15 December 2016)
3 January 2017	30	0.36	20:32:03

207
208

209 **2.4 - Hotplate Gauge**

210   Algorithms used to process hotplate measurements are described in Rasmussen et al.

211 (2011), Boudala et al. (2014), and Zelasko et al. (2018). Henceforth, these are referred to as R11,

212 B14, and Z18, respectively. This section describes how hotplate measurements acquired at the

213 HP site were analyzed. The hotplate deployed at the HP site is described in Wolfe and Snider

214 (2012), Z18, and in Marlow et al. (2023).

215   Five measurements fundamental to the steady state energy budget of the hotplate's

216 temperature-controlled up-viewing plate are output by the hotplate microprocessor as one-minute

217 running averages (Z18). These averages were merged with the GPS time and recorded at 1 Hz by

218 the data acquisition system (Sect. 2.1). With these measurements, calibration data (Marlow et al.

219 2023), and the algorithm developed by Z18, we calculated S in two steps. First, the five hotplate

220 measurements (electrical power supplied to the plate, ambient temperature, wind speed,

221 downwelling shortwave flux, and downwelling longwave flux) were input to Eq. 3 in Z18. The

222 output of that equation is a provisional liquid-equivalent precipitation rate. Second, the snow

223 particle catch efficiency, described in the next paragraph, was used to calculate S as the ratio of

224 the provisional rate and the catch efficiency.

225   Marlow et al. (2023; their Fig. 3b) report the relationship between snow particle catch

226 efficiency and wind speed that was applied in the calculation of S. There are three bases for this

227 relationship. First is the catch efficiencies R11 derived using measurements obtained from a

228 weighing gauge, operated within a double fence intercomparison reference shield, and collocated

229 measurements from an unshielded hotplate gauge. These paired measurements are symbolized

230 SRG (shielded reference gauge) and UHG (unshielded hotplate gauge). R11 plotted hotplate

231 catch efficiencies (i.e., UHG/SRG) versus wind speeds measured at 10 m AGL (their Fig. 8).

232 Second is Marlow et al.'s adjustment of R11's 10 m AGL wind speeds to 2 m AGL. The basis

233 for the adjustment is surface boundary layer parameters derived for R11's site (Kochendorfer et

234 al. 2018) and an equation from Panofsky and Dutton (1984; their Eq. 6.7). The adjustment was

235 made because the hotplate-derived wind speeds, both here and in Marlow et al. (2023), were

236 acquired at approximately 2 m above the snowpack surface. Third is Marlow et al.'s comparison

237 of SNOTEL-derived liquid-equivalent depth changes and hotplate-derived time-integrated

238 accumulations. The interval for the comparisons is 24 hours. Based on the comparison, which

239 has 57 paired values acquired at the sites labeled HP and SN in Fig. 1, the average fractional

240 absolute relative difference is 0.30. Marlow et al. also provided an estimate of the error in a

241 SNOTEL measurement (2.4 mm). At accumulation = 10 mm the error corresponds to a relative

242 error = 0.24. This indicates that SNOTEL contributed significantly to the SNOTEL/hotplate

243 variance and especially so for the smaller accumulations in Fig. 9a of Marlow et al. (2023).

244 Because of this, we do not limit the following estimate of hotplate precision to a subset of the 57

245 paired measurements. Based on our assessment of the average fractional absolute relative

246 difference, the hotplate precision applied in this analysis was taken to be 0.3.

247   The hotplate-derived wind speeds acquired at ~ 2 m, and discussed in the previous

248 paragraph, are henceforth symbolized U_{PRO}. The basis for these is a steady state energy budget of

249 the hotplate's temperature-controlled down-viewing plate and a proprietary algorithm (R11 and

250 Z18). The U_{PRO} are reported by a hotplate as one-minute running averages (Z18) and we

251 recorded these at 1 Hz. Examples are the gray dots in Fig. 2. Additionally, we calculated and

252 analyzed one-minute-averaged values of U_{PRO} and the corresponding standard deviations.

253 Examples of these are the black circles and the short vertical line segments in Fig. 2.

254
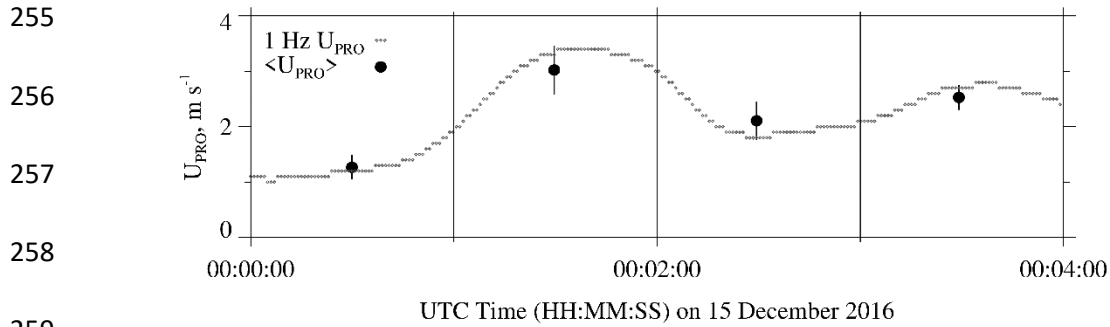
Figure 2 – Hotplate wind speed measurements (U$_{PRO}$) 00:00:00 to 00:04:00 on 15 December

2016. Gray dots are the one-minute running-average U$_{PRO}$ recorded at 1 Hz. Black circles are the

one-minute-averaged U$_{PRO}$ (± 1 standard deviation).

265   **3 - Analysis**

266   **3.1 - WKA Overflight Time**

267   The focus of our analysis is the two WKA flight segments shown in Figs. 3a-b. The maps

268   shown in the figures have the three ground sites (AF, SN, and HP) and the WKA flight tracks

269   (white line). The beginning-to-end time interval for the flight tracks is 100 s and these are

270   divided into ten 10-second intervals. The 10 s intervals are indicated with white diamonds.

271   Except for the turn evident in Fig. 3b, the flight tracks are straight, and the track direction is

272   approximately upwind to downwind.

273   Times that the WKA was closest to the HP site were evaluated by finding the point on the

274   flight track where the horizontal position of the WKA was closest to the hotplate's coordinates.

275   These times are symbolized t_0 and are referred to as overflight times. In Figs. 3a-b the

276   downwind end of the flight tracks end at the overflight time. The latitude/longitude position of

277   the aircraft was within 390 m of the hotplate at the overflight times. Table 1 has the overflight

278   times on the two flight days.

279

280

286
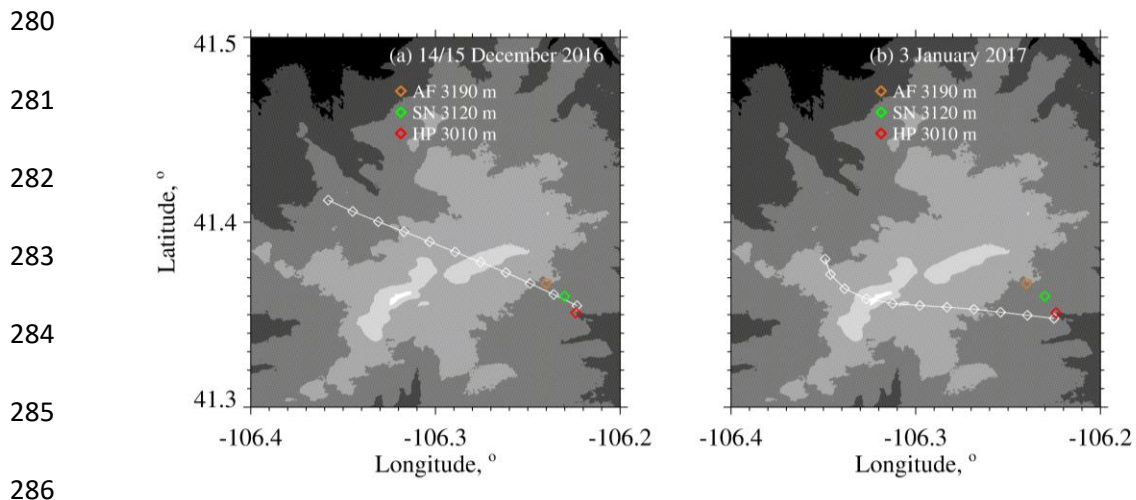
287 Figure 3 – (a) WKA flight track on 14/15 December 2016 for time interval = overflight time -

288 100 s to the overflight time. (b) WKA flight track on 3 January 2017 for time interval =

289 overflight time - 100 s to the overflight time. The white diamonds on the tracks are separated, in

290 time, by 10 s. Altitude thresholds for the digital elevation maps are 2600, 2800, 3000, 3200,

291 3400, and 3600 meters. Altitudes of the ground sites are in the legend.

292

293 **3.2 – Effect of Attenuation on WCR Reflectivities**

294

295   The presence of molecular oxygen, water vapor, cloud water, and snow particles within

296 the WCR's transmission path will contribute to an attenuation of microwave intensity and will

297 therefore negatively bias the retrieved reflectivities (Matrosov 2007; Hiley et al. 2011; Kneifel et

298 al. 2015). Models of attenuation, radar remote sensing, and in situ measurements were used to

299 calculate this bias. For oxygen, an attenuation coefficient from Ulaby et al. (1981; their Fig. 5.6),

300 and temperature (T) and pressure (P) measurements from the AF (Table 2), were used. For

301 vapor, an attenuation coefficient (Ulaby et al. 1981; their Eq. 5.22), and T, P, and relative

302 humidity (RH) measurements from the AF (Table 2), were used. Concentrations of oxygen and

303 water vapor and the oxygen and vapor path lengths are provided in Table 3. The latter is the

304 vertical distance between the HP and the WKA. It was assumed that concentrations were

305 uniform over this path length.

306   Attenuation by cloud water was derived using the WKA-measured T (Table 2), the

307 WKA-measured LWC, path length (Table 3), and an attenuation formula (Liebe et al. 1989; Vali

308 and Haimov 2001). The LWC applied in the formula is the maximum of CDP measurements

309 acquired between t_0 - 10 s and t_0. This interval coincides with the interval the WCR's down-

310 looking antenna was used to acquire reflectivities over the HP (Sect. 3.5). The path length for

311 cloud water was derived as the vertical distance between cloud base [derived thermodynamically

312 using AF measurements (Table 2)] and flight level. LWC was assumed uniform, at the maximum

313 value, over the path length.

314   Snow particle mass concentration is typically reported as an ice water content (IWC, g m^{-}

315 ^{3}) (Liu and Illingworth 2000). The contribution of IWC to attenuation was calculated using

316   measurements in Nemarich et. al (1988), who reported an attenuation coefficient equal to 0.9

317   dB/km per unit of IWC. Also used were retrievals of IWC acquired using the down-pointing

318   WCR antenna. There are several steps in the calculation. First, all profiles of dBZ acquired

319   between t_0 - 10 s and t_0 were selected. Second, a maximum dBZ was selected at each of the

320   down-beam range gates (Table 1). Third, the dBZ maxima were increased by the overall two-

321   way attenuation in the final column of Table 3. Fourth, the profile of attenuation-corrected dBZ

322   was converted to a profile of attenuation-corrected Z. Fifth, a Z-to-IWC parameterization was

323   applied (IWC = $0.10 \cdot Z^{0.51}$; PV11; their Table 3). Sixth, the IWC profile was integrated, and the

324   derived ice water path was divided by the snow particle path length (Table 3). This calculation

325   produced a time- and range-averaged maximum IWC (Table 3). This IWC is the value applied in

326   the attenuation calculation.

327   Two-way attenuations (ΔdB), summed over contributions from the four components, are

328   presented in the final column of Table 3. Attenuation by snow and attenuation by liquid were the

329   most important components (> 50 %) on December 15 and January 3, respectively. Vapor

330   contributed 32 % to the overall on December 15, and the combination of vapor and snow

331   contributed 45 % on January 3. Equation 1 shows how an attenuation-corrected reflectivity (Z')

332   was derived using an uncorrected reflectivity (Z) and the ΔdB.

333

334        $$Z' = 10^{\left[\left[10 \cdot \log_{10}(Z) + \Delta dB\right]/10\right]}$$ (1)

335   Table 2 – Atmospheric state averages

336

Date	WKA [a] Track Altitude, m	WKA [a] T, °C	AF [b] T, °C	AF [b] RH, %	WKA [a, c] Track Vector	WKA [a, c] Wind Vector	AF [b, c] Wind Vector
14/15 December 2016	4546	-13.9	-6.3	86	310 / 130	274 / 32	250 / 8.5
3 January 2017	4196	-21.7	-14.6	77	280 / 120	265 / 27	260 / 5.4

337
338

339   [a] Altitude, temperature, track vector, and horizontal wind vector data obtained by averaging 1 Hz

340   WKA measurements. The averaging interval is 60 s and the interval starts at the overflight time,

341   minus 60 s, and ends at the overflight time.

342

343   [b] Temperature (T), relative humidity (RH), and horizontal wind vector data from sensors on the

344   US-GLE AmeriFlux tower (Sect. 2.1). The wind sensor was deployed at 26 m AGL (3223 m

345   MSL) and the T/RH sensor was deployed at 23 m AGL (3220 m MSL). The AF measurements

346   correspond to 30-minute averages closest to the overpass time. In the AF data set time stamps on

347   the relevant AF recordings are 00:00 UTC (15 December 2016) and 20:30 UTC (3 January

348   2017).

349

350   [c] Vectors are presented in the following format: Direction of motion (degree relative to true

351   north) / speed (m s^{-1}).

352   Table 3 – Attenuating component concentration, one-way pathlength, and the overall two-way attenuation

Date	Conc. Oxygen, kg m^{-3}	Conc. Vapor, kg m^{-3}	Maximum LWC, g m^{-3}	Maximum IWC, g m^{-3}	One-way Pathlength [a] Oxygen, Vapor, and Snow, km	One-way Pathlength [b] Cloud Water, km	Overall Two-way Attenuation, ΔdB
15 December 2016	0.21	2.7x10^{-3}	0.01	0.27	1.54	1.09	1.41 [c]
3 January 2017	0.21	1.3x10^{-3}	0.08	0.09	1.19	0.59	1.01 [d]

353

354   [a] Vertical distance between HP and WKA

355

356   [b] Vertical distance between cloud base [derived thermodynamically using AF measurements (Table 2)] and WKA

357

358   [c] One-way attenuation coefficients are 0.03 dB/km for oxygen (Ulaby et al. 1981), 0.14 dB/km for vapor (Ulaby et al. 1981), 0.056

359   dB/km for cloud water (Liebe et al. 1989; Vali and Haimov 2001), and 0.24 dB/km for snow particles (Nemarich et. al 1988).

360

361   [d] One-way attenuation coefficients are 0.03 dB/km for oxygen (Ulaby et al. 1981), 0.073 dB/km for vapor (Ulaby et al. 1981), 0.49

362   dB/km for cloud water (Liebe et al. 1989; Vali and Haimov 2001), and 0.077 dB/km for snow particles (Nemarich et. al 1988).

363

3.3 - Correction of Doppler Velocity

We accounted for bias in V_D (Sect. 2.3) due to deviation of the down-looking WCR

antenna from vertical. This was done by applying the correction described in Zaremba et al.

(2022) (their Eq. A4). The west-to-east and south-to-north particle velocities used in the

correction were assumed to be equal to component wind velocities. The latter were expressed as

linear functions of altitude using the information in the penultimate and last columns of Table 2.

The component velocities as functions of altitude and the linear equations relating velocity and

altitude are provided in the Appendix.

3.4 - Hotplate Measurement of Wind Speed

Here we compare the hotplate-derived wind speed to wind speed derived using an

R.M.Young rotating anemometer (R.M.Young 2001). The second of these is symbolized U_{RMY}

and the basis for the first (U_{PRO}) is a proprietary algorithm (Sect. 2.4). We are doing this

comparison because B14 showed that U_{PRO} can be high-biased, relative to a conventional

anemometer, and because U_{PRO} is the primary determinant of the rate that the up-viewing plate

dissipates sensible heat energy. Diagnosis of that heat transfer rate is our basis for calculating the

liquid-equivalent snowfall rate (Z18). The U_{PRO} also determines the snow particle catch

efficiency and the latter was used in calculations of the undercatch-corrected liquid-equivalent

snowfall rate (Sect. 2.4).

The comparisons reported here were done at the Laramie, WY Airport in December

2019, and in January 2020. Compared to the HP site, the Laramie Airport site (indicated LA in

Fig. 1) is free of obstruction, out to 120 m, and experiences larger wind speeds. By mounting the

hotplate and the R.M.Young anemometer on rigid metal pipes, the hotplate's heated horizontal

386   surfaces (the up- and down-viewing plates seen in Fig. 1 of Z18) and the anemometer's spinning

387   axis (oriented horizontally) were both positioned at 2 m AGL. The pipes were separated

388   horizontally by 5 m. There was no precipitation on the days selected for the wind speed

389   comparisons. The values of U_{PRO} and U_{RMY} we analyzed were recorded with a data system that

390   time stamped the 1 Hz U_{PRO} and 1 Hz U_{RMY} with a relative timing accuracy no worse than 1 s.

391   A wind speed comparison - from 13 December 2019 - is shown in Fig. 4a. U_{PRO} was

392   brought into the comparison by sampling it once per minute from files containing 1 Hz

393   recordings of the one-minute running-average U_{PRO} (Sect. 2.4). U_{RMY} was brought into the

394   comparison by starting with files containing 1 Hz recordings and converting these to one-minute

395   averages. Fig. 4a shows no evidence of bias and Fig. 4b demonstrates that the average absolute

396   departure between the U_{PRO} and U_{RMY} (both one-minute averages) is no larger than 0.5 m s^{-1}.

397   Table 4 has eight more precipitation-free comparisons. Included in the table are temperature and

398   wind speed averaged over the comparison intervals (4 to 20 UTC), the slope of the linear-least-

399   squares fit line (forced through the origin, red line), and the lower and upper quartiles of the

400   slope. The quartiles were calculated using the method of Wolfe and Snider (2012). In contrast to

401   Figs. 4a-b, Figs. 4c-d make the comparison using 1 Hz values of U_{PRO} and U_{RMY}. The larger

402   scatter and larger average absolute departure seen in these panels is a consequence of the

403   hotplate's limited time response, compared to the R.M.Young. We quantify the hotplate's

404   response time in terms of a calculated thermal response time. During wintertime at the Laramie

405   Airport, and with wind speed at 5 m s^{-1}, the down-viewing plate's thermal response time is

406   approximately 60 s (results not shown). Because the temperature of the down-viewing plate is

407   actively controlled, this does not translate to a 60 s lag between changes in wind speed and the

408   hotplate response. The U_{PRO}/U_{RMY} departure is most evident at U_{PRO} > 5 m s^{-1} (Fig. 4d) but this is

409   not a concern for U_{PRO} on 14/15 December 2016 or on 3 January 2017. Snider (2023)

410   demonstrated that the U_{PRO} was less than 5 m s^{-1} at the hotplate during the two WKA overflights.
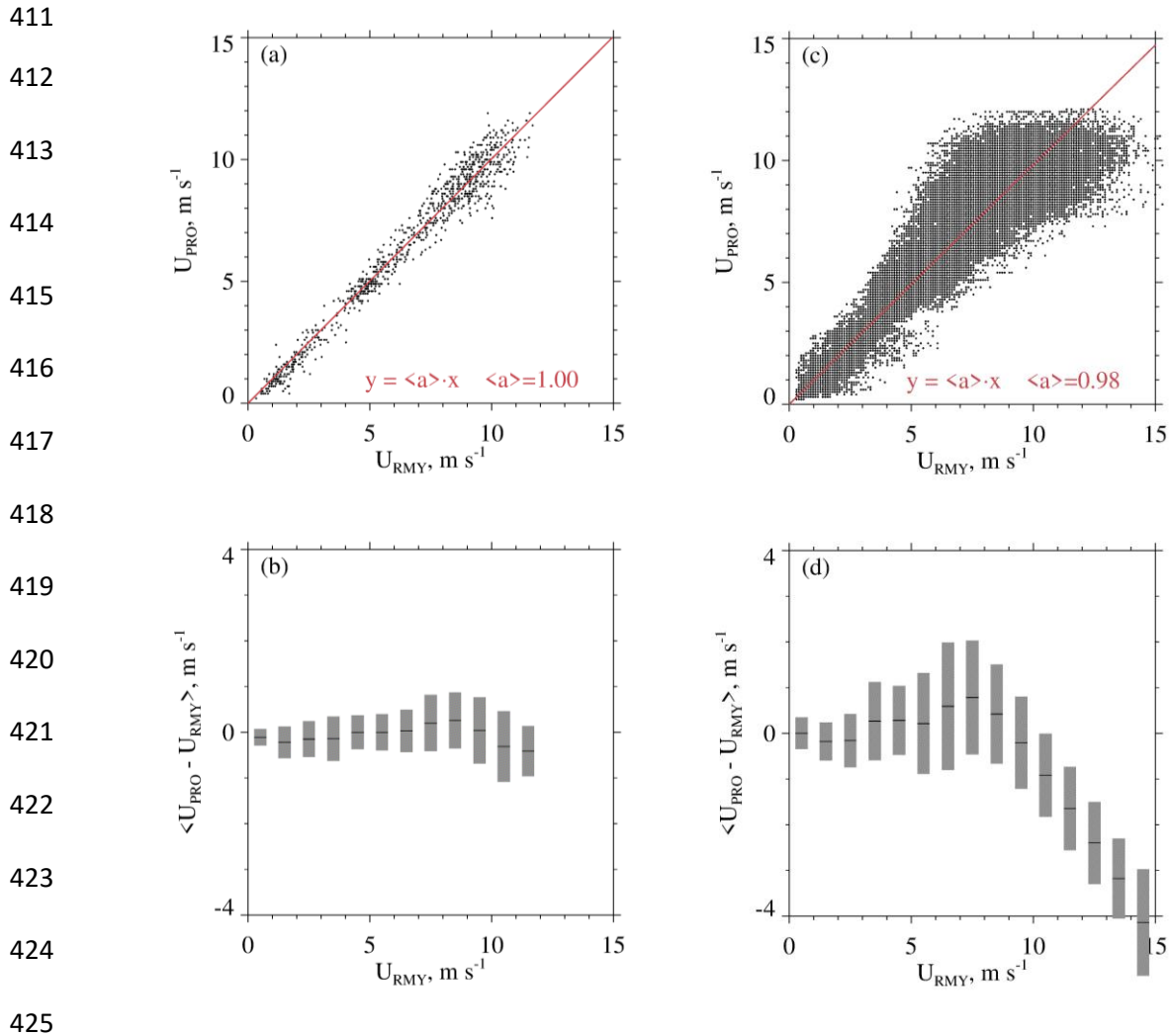
Figure 4 – (a) Scatterplot of one-minute-averaged U_{PRO} and one-minute-averaged U_{RMY}.
Measurements were acquired at the Laramie, WY Airport 13 December 2019. The red line is a
linear-least-squares fit line (forced through the origin). (b) Average departure between one-
minute-averaged U_{PRO} and one-minute-averaged U_{RMY}. Average departures were calculated for
discrete U_{RMY} intervals, and the averages are indicated with short black horizontal lines. Gray
bars indicate $\pm$ 1 standard deviation. (c) Same as in (a) except 1 Hz values of U_{PRO} and U_{RMY}. (d)
Same as in (b) except for 1 Hz values of U_{PRO} and U_{RMY}.

434

435 Table 4 - U_{PRO} versus U_{RMY} correlations

436

Date, UTC [1]	$<T>$ [2], ºC	$<U>$ [2], m s^{-1}	$<a>$ [3]	a [4] First Quartile	a [4] Third Quartile
7 December 2019	-0.40	5.40	1.00	0.90	1.04
8 December 2019	2.70	4.10	0.99	0.90	1.04
10 December 2019	-5.20	3.80	0.99	0.83	1.04
13 December 2019	-1.50	6.60	1.00	0.93	1.06
18 December 2019	-6.20	3.60	0.99	0.92	1.04
19 December 2019	-6.90	2.70	0.95	0.84	0.99
6 January 2020	-6.40	8.80	1.01	0.96	1.06
8 January 2020	0.30	4.20	1.00	0.87	1.05
11 January 2020	-7.20	7.00	1.02	0.97	1.08

437

438

439 [1] Statistics presented are based on one-minute-averaged U_{PRO} and one-minute-averaged U_{RMY}

440 measurements made between 04:00 to 20:00 UTC.

441

442 [2] Interval-averaged temperature and interval-averaged wind speed.

443

444 [3] Slope of the one-minute-averaged U_{PRO} versus one-minute-averaged U_{RMY} linear-least-squares

445 fit line, forced through the origin.

446

447 [4] Quartiles of the slope (see text)

448

3.5 – Combined Aircraft and Surface Measurements

Figure 5 has WCR and WKA measurements starting 100 s prior to t_0 and ending at t_0. The sequences in Figs. 5a and 5c are reflectivities from both the up- and down-looking antennas. In Fig. 5a the flight track (black dashed horizontal line) is at 4550 m and in Fig. 5c the flight track is at 4200 m. At the t_0 in Fig. 5a, below the WKA, the maximum radar echo is +6 dBZ (Z = 4 mm^6 m^{-3}) and in Fig. 5c the maximum is -3 dBZ (Z = 0.5 mm^6 m^{-3}). Supercooled liquid water was detected as the aircraft approached the ridgeline (Fig. 5b) and during the last 10 seconds of the time sequence in Fig. 5d. During these encounters with supercooled liquid, the maximum LWC values were 0.03x10^{-3} and 0.08x10^{-3} kg m^{-3} on 14 December 2016 and 3 January 2017, respectively. Values of N (Sect. 2.2) at times of maximal LWC were 3x10^6 and 100x10^6 m^{-3} on 14 December 2016 and 3 January 2017, respectively. Even on 3 January 2017, the <D> (Sect. 2.2) associated with maximum LWC was sufficient for hexagonal plate crystals with diameter larger than 100 μm to collide with the observed droplets with efficiencies > 0.1 (Wang and Ji 2000).

We temporally and spatially averaged the values of Z we compared with time-averaged values of S. There are two reasons for this: 1) As discussed in Sect. 3.1, the WCR did not sample Z exactly over the hotplate, and furthermore, the width of radar beam at 1500 m range - roughly the distance between the aircraft and the ground at the overflight times - is 30 m and thus considerably smaller than the minimum horizontal distance between the aircraft and the HP. 2) Compared to the WCR, the hotplate is a relatively slow-response measurement system whose output is commonly averaged over one-minute intervals (Z18).
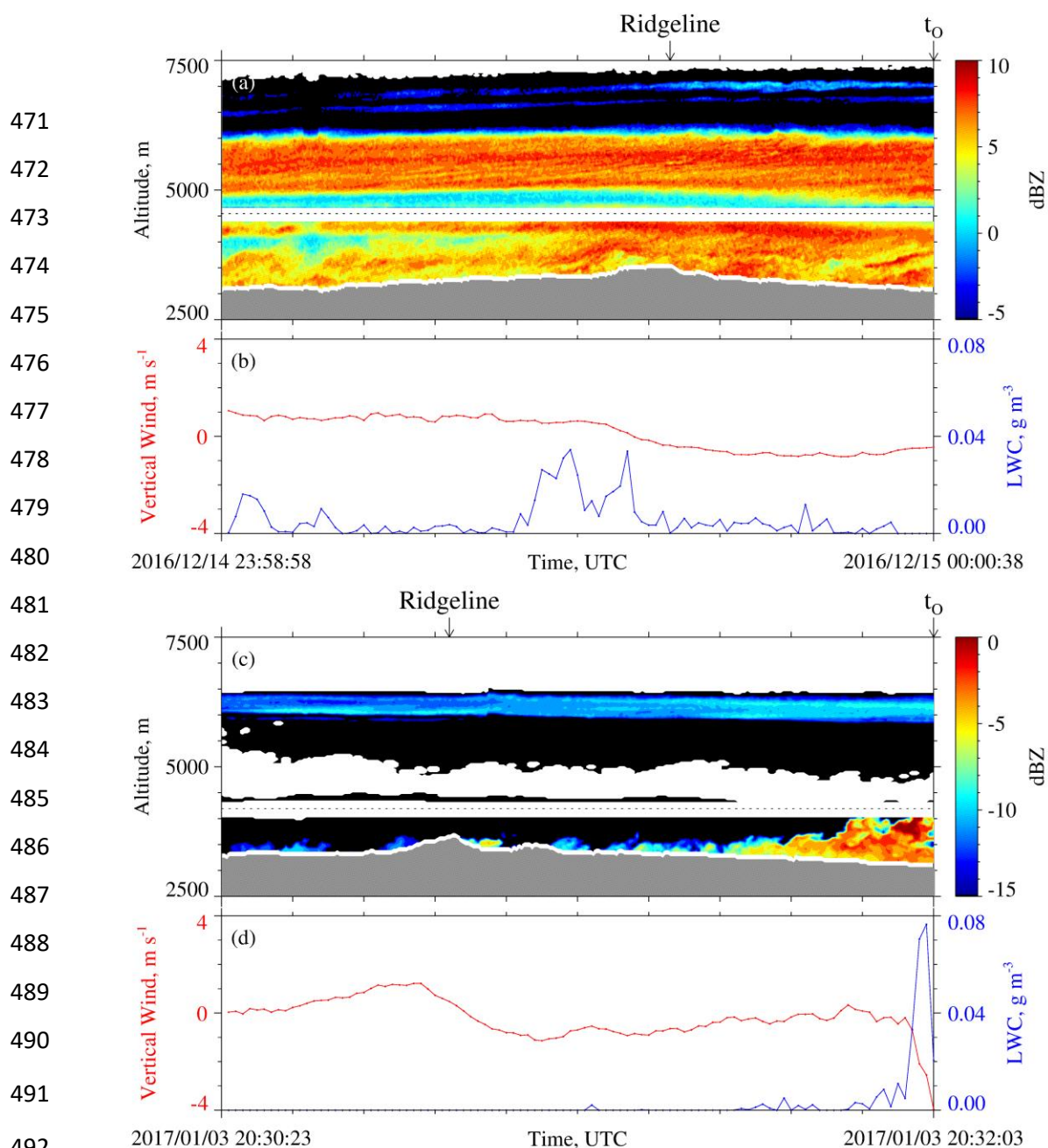
Figure 5 – (a) 100 s of WCR reflectivity and (b) 100 s of LWC and gust probe vertical wind velocity ending at t_0 on 14/15 December 2016. (c) 100 s of WCR reflectivity and (d) 100 s of LWC and gust probe vertical wind velocity ending at t_0 on 3 January 2017. In (a) and (c), above and below the flight track, is the roughly 200-m-deep WCR blind zone, reflectivity above (below) the flight track is from the up-looking (down-looking) WCR antenna, black indicates dBZ values smaller than minimum indicated in the color bar, white immediately above the terrain indicates echo that was discarded because of ground clutter, and white above the ground clutter and outside of the blind zone indicate dBZ < minimum detectable signal.

503   The HP measurements were averaged over two adjacent 60 s intervals. The first extends

504   from t_0 to $t_0 + 60$ s (Fig. 6a) and the second from $t_0 + 60$ s to $t_0 + 120$ s (Fig. 6c). In Fig. 6a and

505   in Fig. 6c, $t_{HP,B}$ symbolizes an interval's beginning time and $t_{HP,E}$ symbolizes an interval's

506   ending time. Formulas describing how these times were related to the beginning and ending time

507   of a corresponding WCR averaging interval are in the Appendix. Fig. 6b is a schematic of the

508   first WCR averaging interval and Fig. 6d is a schematic of the second. Again, the subscripts "B"

509   and "E" are used to indicate averaging beginning and ending times. Figures 6b and 6d both have

510   lines at the top of an averaging interval/domain. The slopes of these lines are proportional to the

511   ratio of two speeds. These speeds are a maximum likely snow particle speed toward the ground (

512   v_p) and a horizontal wind advection speed (v_w). The v_p was calculated using averaged vertical-

513   component Doppler velocities and v_w was calculated using a vertical profile of horizontal winds,

514   based on WKA horizontal wind measurements and AF horizontal wind measurements (Figs.

515   A1a-b), and using the WKA track vector (Table 2). An altitude ($z' = 3400$ m) was assumed in the

516   calculation of v_w . This is the altitude of the ridges west and northwest of the HP site (Figs. 3a-

517   b). Picking the altitude to be either $z' = 3200$ m or $z' = 3600$ m does not alter our findings.

518
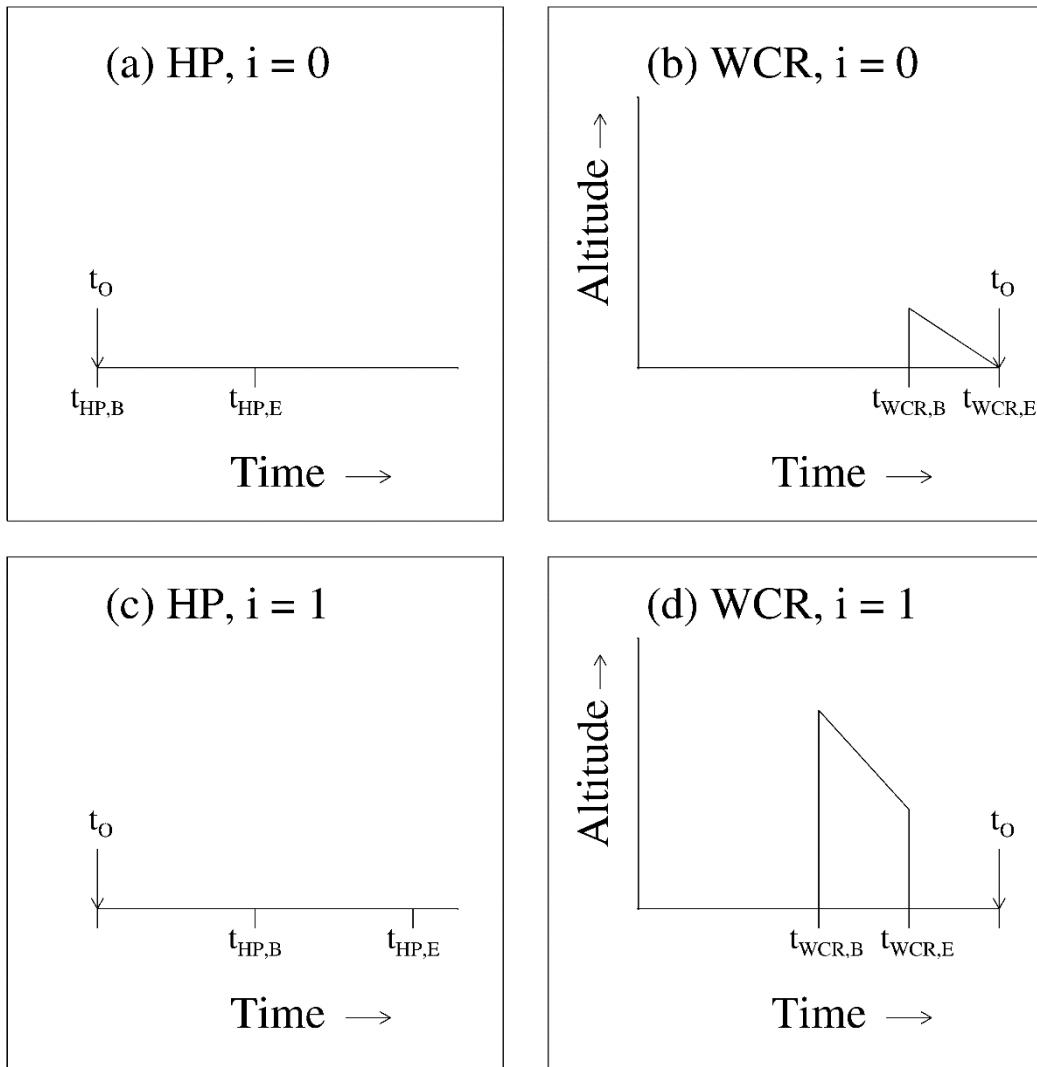
Figure 6 – (a and c) Representations of the $i = 0$ and $i = 1$ HP averaging intervals. (b and d)

Representations of the $i = 0$ and $i = 1$ WCR averaging intervals/domains. The t_o is shown in all

panels. The subscripts "B" and "E" indicate beginning and ending times of HP averaging (panels

a and c) and the beginning and ending times of WCR averaging (panels b and d).

544

545   All panels in Fig. 6 are labeled with an index designating either the first averaging

546   interval ($i = 0$) or the second averaging interval ($i = 1$). Figures 7 and 8 present hotplate

547   snowfall measurements from 14/15 December 2016 and 3 January 2017. In these, and in

548   subsequent figures, colored circles surround the indexes, blue is used to color-code 15 December

549   2016, and red is used to color-code 3 January 2017. Additionally, Fig. 8 has an $i = 2$ averaging

550   interval. This is a special case discussed at the end of this section.

551   Figures 9a-b and Figs. 10a-b have enlarged views of the altitude-time crossections

552   recorded on the two flight days. Different from Fig. 5a and Fig. 5c, these measurements are only

553   from the WCR's down-looking antenna. Additional differences are the following: 1) The plots

554   are set up so that Z and V_D structures downwind of the hotplate can be seen. These structures are

555   discussed in the following section. 2) The WCR measurements are shown for 50 s of flight. With

556   the WKA ground speed approximately 125 m s^{-1} (Table 2), the distance along the abscissa is

557   6250 m. 3) Colored circles that surround the $i = 0$ index are placed below the WCR averaging

558   intervals/domains. The latter are drawn with solid black lines and are seen to overlay both the Z

559   and V_D altitude-time crossections. Consistent with Figs. 6b and 6d, and the Appendix, one of

560   these black lines is vertical and the other is negatively sloped. Figs. 10a-b also have the $i = 2$

561   intervals/domains discussed at the end of this section.

562
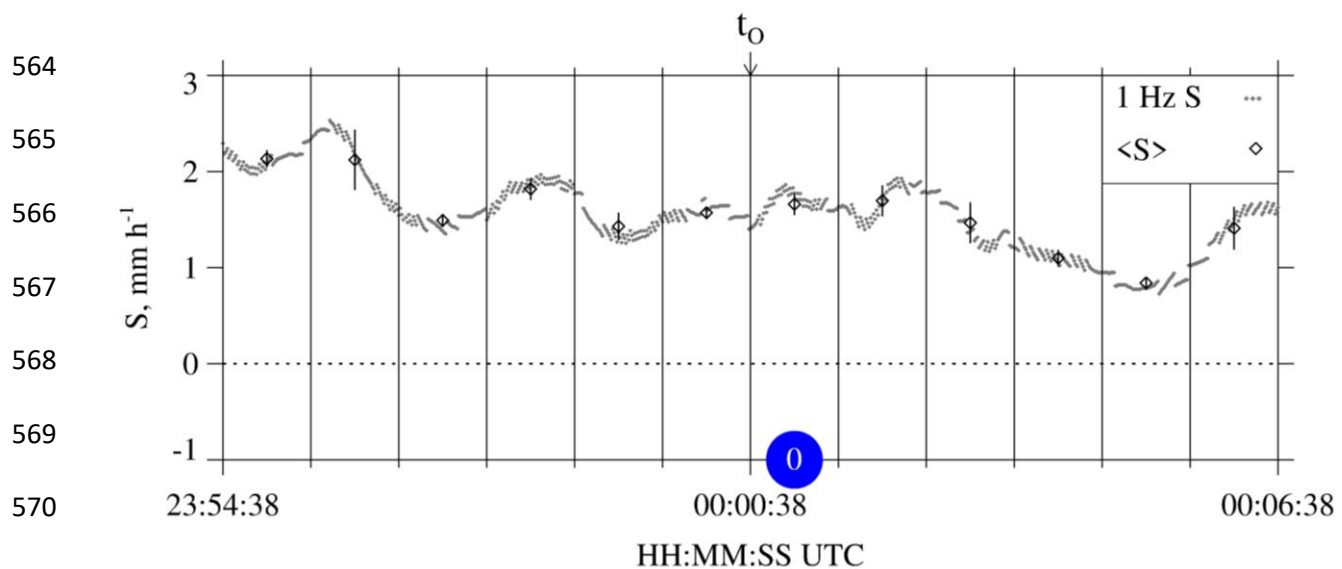
563

Figure 7 – Twelve minutes of HP snowfall measurements from 14/15 December 2016. Gray dots

are S values calculated using hotplate output recorded at 1 Hz. Black diamonds are the one-

minute-averaged values (± 1 standard deviation). The t_0 is shown above the panel and the blue

circle designates the $i = 0$ HP averaging interval.

578

579

580

581

582

583

584

585

586

587
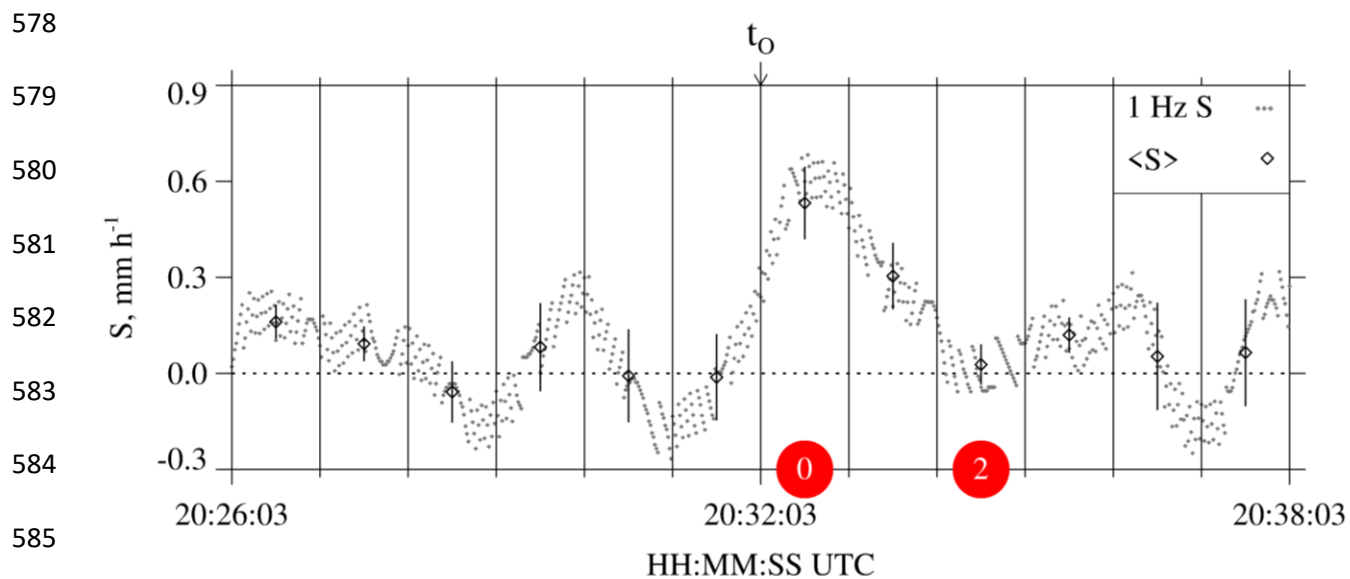
588 Figure 8 – Twelve minutes of HP snowfall measurements from 3 January 2017. Gray dots are S

589 values calculated using hotplate output recorded at 1 Hz. Black diamonds are the one-minute-

590 averaged values (± 1 standard deviation). The t_o is shown above the panel, a red circle designates

591 the $i = 0$ HP averaging interval, and a red circle designates the $i = 2$ HP averaging interval. The

592 latter is a special case discussed at the end of Sect. 3.5.

593

594

595

596

597

598

599

600

601

602

603

604

605

606

607
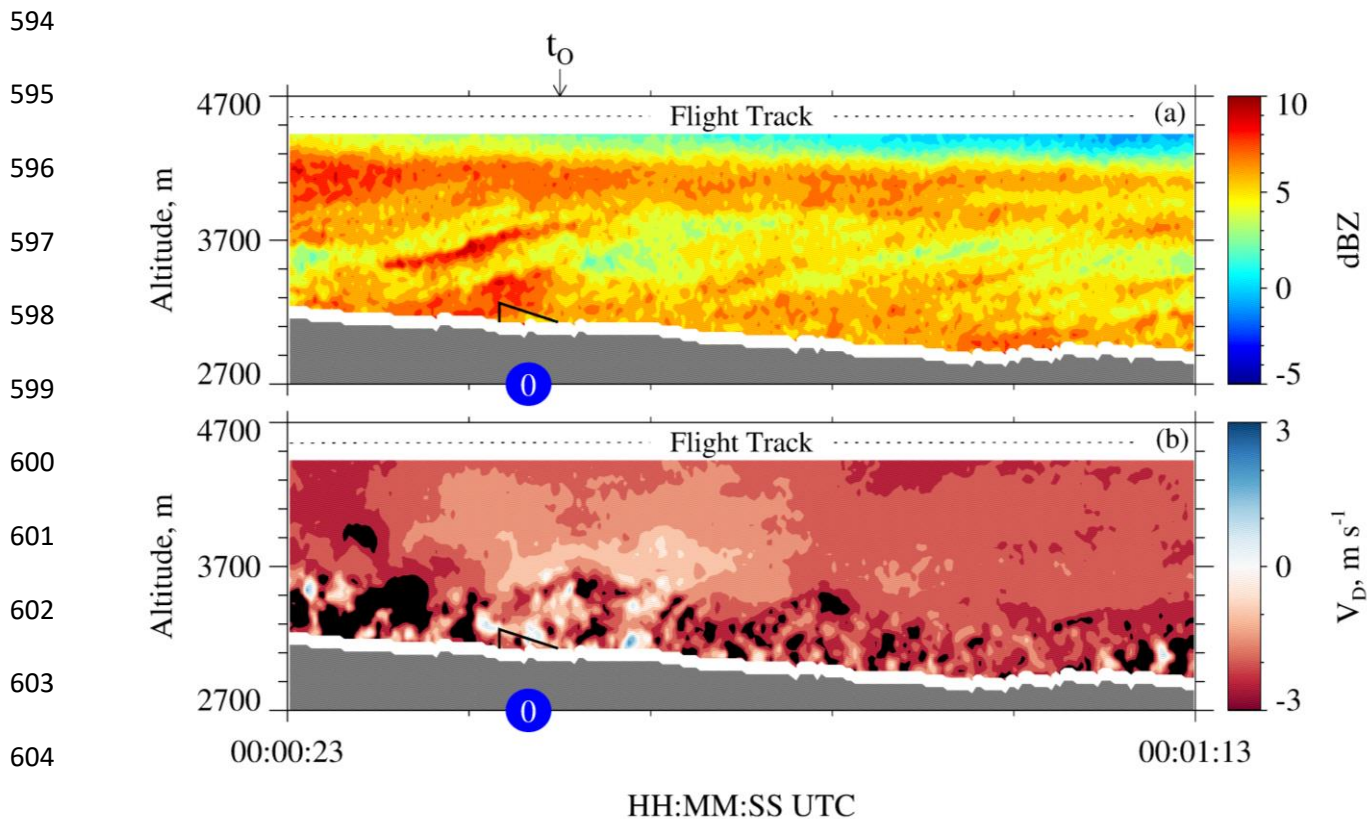
608   Figure 9 – 50 s of measurements from the down-looking WCR antenna on 15 December 2016.

609   (a) Crossection of reflectivity t_0 - 15 s to t_0 + 35 s. (b) Crossection of Doppler velocity t_0 - 15 s to

610   t_0 + 35 s. The t_0 is shown above the top panel. In both panels, the solid black lines (vertical and

611   sloped) encompass the $i = 0$ WCR averaging interval/domain and blue circles designate the

612    $i = 0$ WCR averaging interval.

613

614
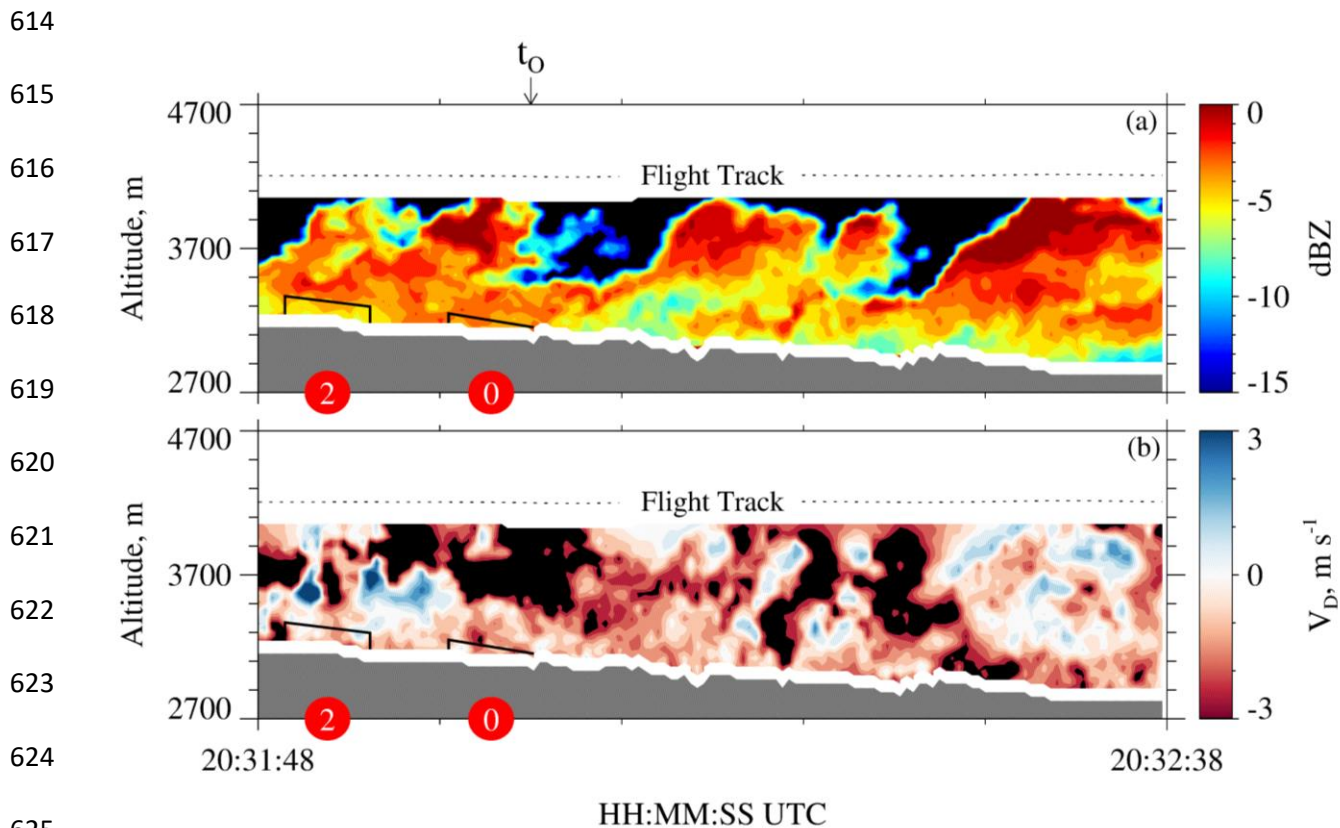
627 Figure 10 – 50 s of measurements from the down-looking WCR antenna on 3 January 2017. (a)

628 Crossection of reflectivity t_o - 15 s to t_o + 35 s. (b) Crossection of Doppler velocity t_o - 15 s to t_o

629 + 35 s. The t_o is shown above the top panel. In both panels, the solid black lines (vertical and

630 sloped) encompass the $i=0$ and $i=2$ WCR averaging intervals/domains, two red circles

631 designate the $i=0$ WCR averaging interval, and two red circles designate the $i=2$ WCR

632 averaging interval. The $i=2$ intervals/domains are a special case discussed at the end of Sect.

633 3.5.

634

635   The $i = 0$ averages of S and Z are presented in Table 5 and the corresponding averaging

636   intervals are viewable in Fig. 7 and Fig. 9a (15 December 2016) and in Fig. 8 and Fig. 10a (3

637   January 2017). The $i = 1$ averages are also presented in Table 5. According to the averaging

638   scheme (Fig. 6), the $i = 1$ HP averaging interval is time-shifted positively compared to the $i = 0$

639   HP averaging interval and the $i = 1$ WCR averaging interval is time-shifted negatively compared

640   of the $i = 0$ WCR averaging interval. This arrangement of the averaging intervals is one way to

641   average while also accounting for wind advection of the snow particles.

642   As discussed earlier in this section, the averaging scheme initializes with 60-second

643   blocks of HP data between t_0 and $t_0 + 120$ s. When we applied the scheme to data from 3 January

644   2017, but outside the specified time range, an inconsistency was documented. This is apparent in

645   Fig. 8, where the $t_0 + 120$ s to $t_0 + 180$ s interval (i.e., the $i = 2$ interval) has negligible average S,

646   while in Fig. 10, the $i = 2$ interval has a non-negligible average Z (~ 0.3 mm^6 m^{-3}). A firm

647   explanation is not available for the inconsistency, but a factor may be the convective nature of

648   the fields in Figs. 10a-b. Because of the inconsistency, only averages corresponding to the $i = 0$

649   and $i = 1$ intervals were analyzed further.

650

651

652 Table 5 – Averaged wind, hotplate, and WCR measurements

Date	v_w [a], m s^{-1}	i index	$<S>\pm\sigma_S$ [b], mm h^{-1}	WCR Samples [c]	$<V_D>$ [d], m s^{-1}	σ_{V_D} [e], m s^{-1}	v_p [f], m s^{-1}	$<Z>\pm\sigma_Z$ [g], mm^6 m^{-3}
15 December 2016	7.4	0	1.7±0.1	42	-1.3	0.9	2.2	4.9±2.1
15 December 2016	7.4	1	1.7±0.2	149	-1.8	1.2	3.0	5.6±1.1
3 January 2017	8.9	0	0.5±0.1	22	-0.9	0.8	1.7	0.49±0.05
3 January 2017	8.9	1	0.3±0.1	35	-0.8	0.4	1.2	0.50±0.10

653

654 [a] Horizontal wind advection speed (Eq. A7) calculated using values from the penultimate and last

655 columns of Table 2.

656

657 [b] One-minute average of the undercatch-corrected liquid-equivalent snowfall rate ($\pm$ 1 standard

658 deviation). An example averaging interval is the interval in Fig. 7.

659

660 [c] Number of samples used to calculate WCR statistics in the penultimate four columns. The

661 averaging intervals/domains (e.g., $i = 0$ in Figs. 9a-b and in Figs. 10a-b) encompass the averaged

662 WCR samples.

663

664 [d] Average of Doppler velocity within the averaging intervals/domains.

665

666 [e] Standard deviation of Doppler velocity within the averaging intervals/domains.

667

668 [f] Maximum likely snow particle speed toward the ground (Eq. A8).

669

670 [g] Average reflectivity ($\pm$ 1 standard deviation). These values are not corrected for attenuation.

671

672 **3.6 - Snow Particle Imagery**

673   In Fig. 9a and Fig. 10a, the time for a snow particle to move the abscissa and ordinate

674 distances is different. The ratio of these two times is 2.6. This follows from our choice of

675 abscissa and ordinate ranges, from values of particle fall speed (1 m s^{-1}) and horizontal wind

676 advection speed (8 m s^{-1}), which we assumed, and from the WKA ground speed ($gs \sim 125$ m s^{-1};

677 Table 2). The assumed values are approximately consistent with values of $<V_D>$ and v_w, in

678 Table 5, and with the V_D sign convention (Sect. 2.3). We also used $gs = 125$ m s^{-1} to scale

679 (virtually) the time axes in Fig. 9a and Fig. 10a to a horizontal distance. Within the scaled

680 coordinate frames, we assumed that all snow particle trajectories have negative slope ($\Delta z / \Delta x = $ -

681 1 m s^{-1} / 8 m s^{-1} = -0.12) and that all trajectories are stationary. However, both assumptions seem

682 inconsistent with the reflectivity structures in Fig. 5a, where positively-sloped particle fall

683 streaks are evident at $\sim$ 5500 m, inconsistent with Fig. 9a where positively-sloped fall streaks are

684 at $\sim$ 3500 m, and inconsistent with the positively-sloped fall streaks in Fig. 10a. On both flight

685 days, the fall streaks evince particle sources that move horizontally and with a horizontal speed

686 that is larger than the $v_w = 8$ m s^{-1} applied in the estimate of the trajectory slope. It may be that

687 the source's horizontal speed is comparable to the flight-level WKA-derived horizontal wind (27

688 to 32 m s^{-1}; Table 2) but we do not have data needed to verify that assertion. Based on the

689 assumption that snow particles followed the fall streaks while both were advecting horizontally,

690 we looked *downwind* of the hotplate - at a time later than t_0 in Fig. 9a and Fig. 10a - for particles

691 that became those that produced snowfall at the hotplate.

692   Particle images from 15 December 2016 were analyzed using the 2DP. With this

693 instrument the maximum all-in particle size (in the horizontal direction perpendicular to flight) is

694   6400 μm and the particle size resolution is 200 μm (Sect. 2.2). Within the time interval picked

695   for this analysis (discussed below), particles sizing in the smaller of the two spectral modes, with

696   mode size ~ 400 μm, were more numerous (results not shown). Because the 400 μm particles are

697   poorly resolved by the 2DP, and the same can be said for somewhat larger particles, those

698   smaller than 1000 μm were excluded from the following analysis. Figure 11a shows imagery

699   from 12 s of measurements acquired near the end of the sequence in Fig. 9a (00:01:02 to

700   00:01:14). This time interval was selected by tracing forward from t_0, along the slope of the fall

701   streaks, to the flight level. Many of the particles are rounded (indicating riming) and a few have

702   arms likely due to incomplete conversion of branched crystals to rimed snow particles. The mode

703   size corresponding to these images is 1600 μm. No liquid water was detected with these particles

704   (LWC < 0.01x10^{-3} kg m^{-3}; Fuller 2020; her Fig. 8), but liquid was detected, at ~ 00:00:00, as the

705   aircraft approached the ridgeline (Figs. 5a-b).

706   Turning to imagery from 3 January 2017, the most appropriate location for analysis

707   would be through the second billow structure evident in Fig. 10a. This billow sourced a fall

708   streak that terminated at the hotplate (i.e., at the time t_0 indicated in the figure). However, the

709   aircraft only clipped the top of this billow, and it was only when sampling the billow seen ~ 13 s

710   earlier that larger ice particle concentrations (~ 20,000 m^{-3}) (Fuller 2020; her Fig. 10) and larger

711   LWC (~ 0.08x10^{-3} kg m^{-3}; Fig. 5d) were detected. Maximum reflectivities were the same in all

712   three billows (Z ~ 1 mm^6 m^{-3}; 0 dBZ), so it was assumed that imagery collected in the first

713   billow (20:32:00 to 20:32:02) was representative of what was falling toward the hotplate. The

714   2DS was used to image these particles (Fig. 11b); with this instrument the maximum all-in

715   particle size (in the horizontal direction perpendicular to flight) is 1280 μm and the size

716   resolution is 10 μm (Sect. 2.2). Most of the objects in Fig. 11b appear to be rimed and their mode

717   size is ~ 400 μm. It is also noted that particles smaller than 100 μm were eliminated from these

718   images, however, compared to the ~ 400 μm particles those smaller than 100 μm were

719   significantly less abundant (results not shown).

720

721 (a)

728 (b)
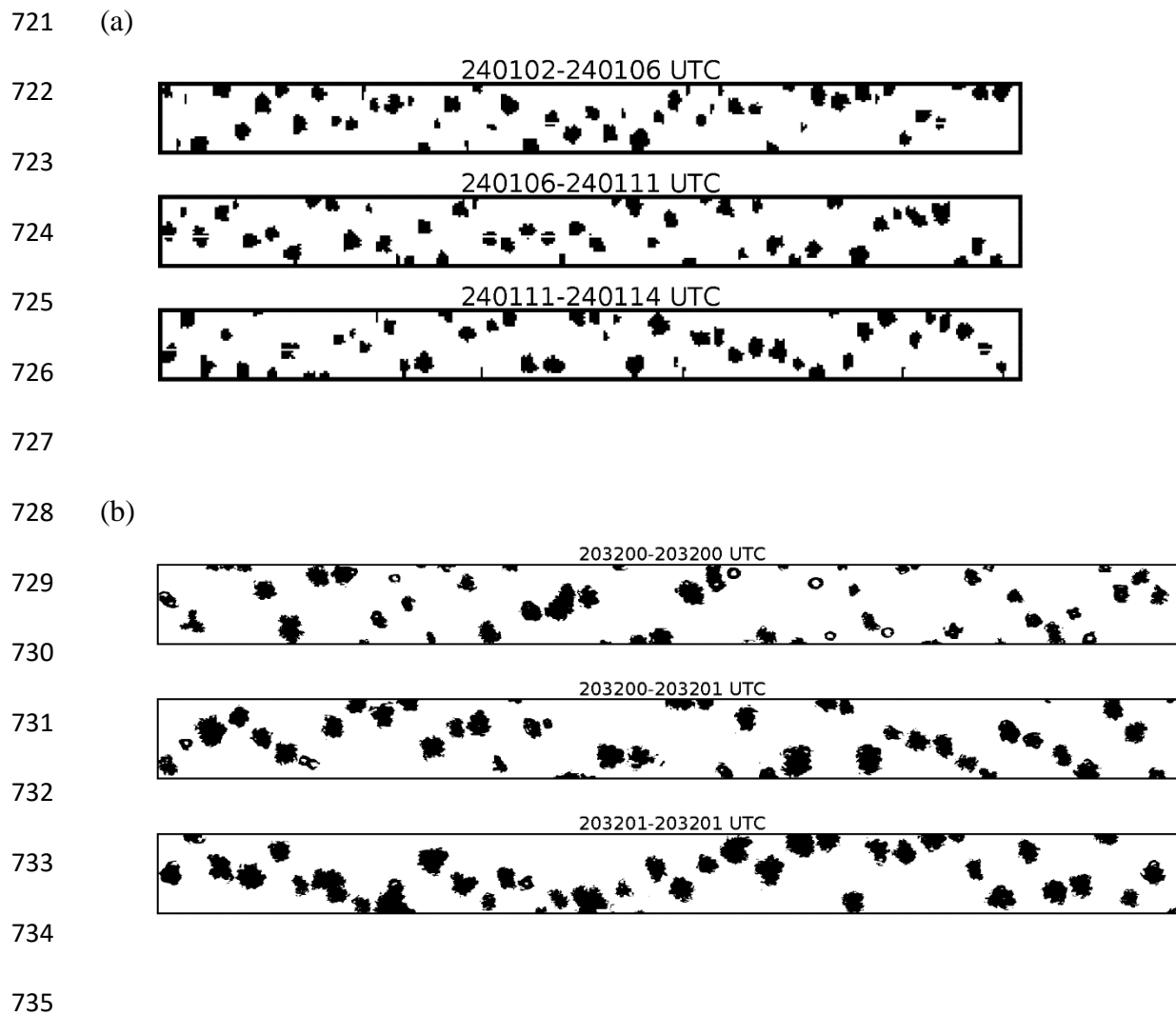
736 Figure 11 – (a) 2DP particle imagery from 15 December 2016. The height of the strips is 6400

737 μm. These particles are estimated to be representative of those that fell from flight level toward

738 the hotplate. (b) 2DS particle imagery from 3 January 2017. The height of the strips is 1280 μm.

739 These particles are estimated to be representative of those that fell from flight level toward the

740 hotplate.

741

3.7 – S/Z Relationships

742

743   Our S/Z pairs are presented in Table 5 where the indexes ($i = 0$ and $i = 1$) are used to

744 indicate results derived for the averaging intervals. In Table 5, reflectivities are not corrected for

745 attenuation, however, in Fig. 12a, attenuation-corrected reflectivities are plotted. Reflectivities

746 from Table 5, attenuations from Table 3, and Eq. 1 were used to calculate the corrected

747 reflectivities. Also shown is a subset of the S/Z pairs from PV11's Fig. 11 ($0.01 < Z < 10$ mm^6

748 mm^{-3}) and the PV11 best-fit line (black). Results from PV11 are specified as S(ρ_1)/Z because

749 those authors applied the lower of two density-size functions (ρ_1), and the lower of two fall

750 speed-size functions, with airborne measurements, in calculations of snowfall rates (Sect. 1).
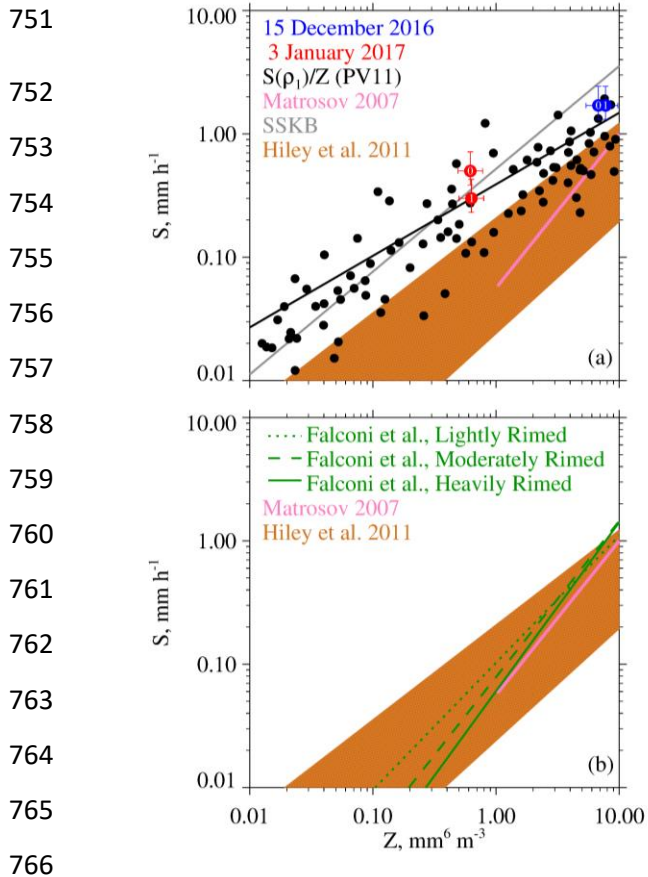
Figure 12 – a) Snowfall rate versus radar reflectivity. Colored circles indicate attenuation-corrected reflectivities (Table 3, Table 5, and Eq. 1) for the $i = 0$ and $i = 1$ averaging intervals. Error bars on these points represent the precision of the Z measurement (Sect. 2.3) and the precision of the S measurement (Sect. 2.4). The $S(\rho_1)/Z$ points are a subset from PV11's Fig. 11 $(0.01 < Z < 10$ mm^6 mm$^{-3})$. Also plotted is the PV11 best-fit line (black) (Sect. 1), the S/Z relationship from Matrosov (2007) (Sect. 1), the S/Z relationship abbreviated SSKB (Sect. 1), and the swath of S/Z relationships from Hiley et al. (2011) (Sect. 1). b) S/Z relationships from Falconi et al. (2018) (their Table 2) (Sect. 1), the Matrosov (2007) relationship, and the swath of S/Z relationships from Hiley et al. (2011) are shown.

778   There are two potential biases in the values of S we measured (Table 5) and plot (Fig.

779   12a). First, the two snowfall events had flight-level vertical wind velocities that were positive

780   (upward) upwind of the summit, and vice versa downwind of the summit. Except for the

781   strongest downdraft on 3 January 2017, the magnitude of this variance is ~ 1 m s^{-1} (Figs. 5b and

782   5d). Assuming 1 m s^{-1} was the downward wind immediately over the hotplate, the snow particles

783   would have approached the gauge faster than their fall speed. Our basis for stating this is fall

784   speeds for the mode sizes discussed in Sect. 3.6 (1600 and 400 μm) and our assumption that the

785   particles were graupel. (Table 6 has these characteristic sizes and fall speeds.) However, the

786   conjectured downdraft speed is likely an overestimate - because of divergence occurring as the

787   draft approached the surface - and because the sizes in Table 6 likely underestimate what fell to

788   the hotplate. Relevant to the last of these assertions, we used the altitude/T/RH measurements

789   (Table 2) to calculate the vertical distance available for growth via riming, and thus for a fall

790   speed increase, between the flight level and the lifted condensation level. Assuming an

791   adiabatically-stratified liquid cloud and unit collection efficiency (these assumptions

792   overestimate growth by riming), and no change of particle crossection (underestimates growth by

793   riming), our calculations indicate that relative increases of size and fall speed were 40 and 20 %,

794   respectively, on 3 January 2017, and that these relative increases were a factor-of-two larger on

795   15 December 2016.

796

797   Table 6 – Estimates of snow particle fall speed

Date	Mode Size, μm	Assumed Particle Type	Fall Speed, m s^{-1}	Reference
15 December 2015	1600	graupel	1.4	PV11; assuming ρ_1 in their Fig. 5
3 January 2016	400	graupel	0.7	PV11; assuming ρ_1 in their Fig. 5

798
799

800   Second, there is concern that values of S from 3 January 2017 are underestimated.

801   Although values of S must be > 0, we presented 1 Hz values (gray points, Fig. 8) approaching -

802   0.3 mm h^{-1}. Negative values resulted because we did not impose a threshold of 0 mm h^{-1} on the

803   uncorrected snowfall rates (this thresholding is discussed in Z18) and because negative snowfall

804   rate values (uncorrected for catch inefficiency) are amplified by the gauge-catch correction (Sect.

805   2.4). The implication is that 0.2 mm h^{-1} could be added to the one-minute averaged values of S in

806   Table 5 and in Fig. 12a. Here, the assumption is that an averaged S of -0.2 mm h^{-1}, in Fig. 8, is

807   indicating no snowfall at the hotplate; however, because the hotplate was operated autonomously

808   (Sect. 2.1) we have no way to verify the assumption.

809

810   **4 – Results**

811   Figure 12a shows the four S/Z pairs (red and blue circles, our measurements) after the

812   reflectivities were corrected for attenuation. The error bars on these data pairs represent the

813   precision of the Z measurement (Sect. 2.3) and the precision of the S measurement (Sect. 2.4).

814   Presentation clarity was what guided the selection of S and Z axis ranges in this figure but with

815   the consequence that 32 of PV11's S/Z pairs are not shown because they plot at $Z > 10$ mm^6 m^{-3}.

816   The way that the PV11 data pairs scatter closest to $Z = 10$ mm^6 m^{-3}, combined with the fact that

817   the PV11 data points at $Z > 10$ mm^6 m^{-3} are not shown, could lead to the interpretation that the

818   slope describing the best-fit relationship at Z approximately > 2 mm^6 m^{-3} should be decreased

819   relative to the slope of the PV11 best-fit line. Readers who view PV11's Fig. 11 will conclude

820   that this interpretation is not warranted. The four S/Z pairs (red and blue circles) plot above the

821   PV11 best-fit line but within the variability of PV11's S/Z pairs.

822   Computational S/Z relationship have inputs from parameterized descriptions of density,

823   shape, fall speed, PSD, and particle size (Sect. 1). Matrosov (2007) did calculations for the snow

824   particle type known as aggregates. Hiley et al. (2011) did calculations for 20 snow particle types.

825   Except for a S/Z calculation done for aggregate snowflakes, the calculations of Hiley et al.

826   (2011) were for the particle type known as vapor-grown crystals. Hiley et al. (2011) did not

827   model spherical snow particles. The latter were modeled by Surussavadee and Staelin (2007) and

828   Kulie and Bennartz (2009). In Fig. 12a, the abbreviation SSKB is used to symbolize the

829   computational S/Z relationship for spherical snow particles.

830   Fig. 12a shows the separation between our S/Z pairs and the Matrosov (2007) calculation.

831   The separation is about a factor of two for the points obtained on 15 December 2016. The points

832   obtained on 3 January 2017 plot at a Z smaller than the lower-limit of the calculation. Since the

833   particle images (Fig. 11a-b) reveal no evidence for the particle type modeled by Matrosov (2007)

834   (aggregate snowflakes), it is not surprising that the calculation is not representative of our

835   measurements.

836   Departures between our S measurements (Fig. 12a) and S/Z calculations from Hiley et al.

837   (2011) were evaluated as the vertical distance between the top of the orange region and our S/Z

838   data pairs. Snowfall rates at the top of the orange region were calculated using attenuation-

839   corrected reflectivities (Eq. 1 and Table 5) and using the upper-limit S/Z equation from Hiley et

840   al. (2011) ($S = 0.21 \cdot (Z')^{0.77}$; Sect. 1 and Eq. 1). The departures were evaluated as a relative

841   difference expressed as $(S_{HP}-S)/S$ with S_{HP} one of four snowfall rates from Table 5. The relative

842   difference is no smaller than 0.7 and 1.0 on 15 December and 3 January, respectively. These

843   minimum relative differences exceed the hotplate precision (Sect. 2.4) by at least a factor of two.

844   It is concluded that our paired values of surface-measured precipitation rate and aircraft-

845   measured radar reflectivity, after correcting for attenuation, provide evidence that a calculation

846   of S based on the Hiley et al. (2011) upper-limit, when applied to rimed snow particles, is

847   associated with a low-biased estimate of S.

848   A plausible explanation for the low bias is the smaller density implicit in most

849   computationally-based S/Z relationships and especially those which assume that snow particles

850   are crystals. Densities are quite different for crystals versus that for rimed snow particles. For

851   example, in Brown and Francis (1995), assuming a 2 mm crystal, the density is ~ 30 kg m^{-3},

852   whereas in PV11 (their Eq. 1), assuming a 2 mm graupel particle, the density is ~ 200 kg m^{-3}.

853   Fig. 12a also has the SSKB relationship. This was developed using density = 200 kg m^3 (Sect. 1).

854   Compared to S/Z relationship represented by top of the orange region in Fig. 12a, the SSKB line

855   plots closer to our data points and closer to many of those reported by PV11.

856   Based on data from PV11 and our result, as well as the S/Z relationship abbreviated

857   SSKB (Sect. 1), it is expected that the S/Z relationships reported by Falconi et al. (2018) for

858   rimed snow particles (Sect. 1) would plot higher in S-versus-Z space than illustrated in Fig. 12b.

859   Notably, only the upper-end of the Falconi et al. lines ($Z > 8$ mm^6 m^{-3}) plot above the upper limit

860   that Hiley et al. (2011) established for unrimed snow particles. A plausible explanation for the

861   lower-than-expected S/Z relationships of Falconi et al. is now offered. Falconi et al. used liquid

862   water path as a proxy for the extent of snow particle riming (von Lerber et al. 2017). A

863   consequence may have been that the proxy did not dependably exclude unrimed snow particles

864   (crystals and aggregates) from the riming categories of Falconi et al. If this was true, then the

865   data groupings that were the basis for the Falconi et al. S/Z relationships may have been affected.

866   Further research is needed to resolve the reason for the mismatch between S/Z pairs, reported

867   both here and in PV11, and the S/Z relationships reported in Falconi et al.

868   Our conclusion that the upper-limit S/Z relationship from Hiley et al. (2011)

869   underestimates S would be modified if our WCR-derived reflectivities were negatively biased.

870   Assuming the reflectivities are negatively biased by 2.5 dBZ, the minimum relative differences

871   discussed previously are no smaller than 0.1 and 0.3 on 15 December and 3 January,

872   respectively. A bias in reflectivity of this magnitude cannot be ruled out but neither can a

873   positive bias of the same magnitude (Sect. 2.3). The latter increases the minimum relative

874   differences to 1.6 and 2.2 on 15 December and 3 January, respectively. In each of these

875   calculations we have summed the attenuations (Table 3) with ± 2.5 dBZ and used Eq. 1 to

876   calculate error-perturbed reflectivities.

877   The scatter of measurements in Fig. 12a, the plausibility of a -2.5 to +2.5 dBZ bias in

878 WCR reflectivity measurements, and error in measurement of S (Sect. 2.4), indicate that refined

879 techniques will be needed in future investigations which apply the approach described here.

880 Additionally, improved methods are needed to diagnose situations where riming is occurring

881 within clouds. Both lidars and radiometers can sense supercooled liquid water from space (e.g.,

882 Battaglia and Panegrossi, 2020), and if combined with Doppler radar, can diagnose precipitation

883 attributable to rimed snow particles. These approaches are being tested in ground-based field

884 studies (Kneifel et al. 2015; Moisseev et al. 2017; Mason et al. 2018) but are most reliable in

885 scenarios with the magnitude of vertical air speed smaller than particle fall speed.

886 **5 - Conclusions**

887   The reported measurements consist of surface measurements of S and near-surface

888 measurements of Z. The latter came from overflights of a ground site, where a precipitation

889 gauge was operated, and were acquired using an airborne W-band radar. The values of Z were

890 corrected for attenuation. The reported S/Z pairs plot at or above the S-versus-Z best-fit line of

891 PV11. However, the points do not depart beyond the variability evident in a replotting of S/Z

892 pairs from PV11. The PV11 data came from airborne measurements of W-band reflectivity,

893 acquired within ± 100 m of flight level, and from coincident measurements of snow particle

894 imagery. PV11 used a density-size function and a fall speed-size function, and measurements

895 (PSD and particle images) to calculate S.

896   There is an offset between the S points, reported here, and reflectivity-dependent S values

897 calculated at an upper-limit S/Z relationship for unrimed snow particles (Hiley et al. 2011). The

898 offset is larger than the precision of the S measurement. This suggests that a measured Z and the

899 Hiley et al. (2011) upper limit will produce an underestimate of precipitation in scenarios

900 dominated by rimed snow particles.

901   New research is needed to refine the S/Z relationship for rimed snow particles. This could

902 be computational – e.g., investigating the utility of parameterizing S in terms of both Z and

903 density – or could be observational. Unlike the investigation of PV11, where only an airborne

904 platform was employed, we have demonstrated that useful information can be obtained using

905 coordinated ground-based and airborne systems. Another approach would be with only ground-

906 based instrumentation. This would avoid some of the complications encountered in this study,

907 including W-band attenuation and a reliance on particle imagery acquired aloft. A study with

908 both ground-based and airborne systems would be useful for understanding a S/Z mismatch,

909 apparent at $Z < 8$ mm^6 m^{-3}, and which is larger than the offset summarized in the previous

910 paragraph. Elements of the mismatch are the S/Z measurements reported by PV11, the

911 measurements reported here, and the measurement-based S/Z relationships reported by Falconi et

912 al. (2018). These three research teams reported measurements relevant to the development of a

913 S/Z relationship for rimed snow particles.

914 **6 - Appendix**

915   This appendix explains how HP (hotplate) and WCR (Wyoming Cloud Radar) averages

916 were evaluated. The scheme starts with an HP averaging interval (duration 60 s) and derives a

917 WCR averaging interval and a WCR averaging domain. The latter encompasses a subset of the

918 altitude-time crossection sampled by the WCR. The top boundary of the domain was derived

919 using vertical-component Doppler velocities within the interval/domain. Because of this

920 dependence, the line defining the top boundary had to be derived iteratively.

921   With the overflight time symbolized t_O, the beginning and ending times of the first of

922   two 60-second HP averaging intervals are

923        $$t_{HP,B} = t_O \qquad\qquad\qquad\qquad\text{(A1)}$$

924        $$t_{HP,E} = t_O + 60 \qquad\qquad\qquad\qquad\text{(A2)}$$

925   Since two adjacent HP averaging intervals are evaluated in this analysis, we express the

926   averaging times with the following recursive equations

927        $$t_{HP,B}(i) = t_O + i \cdot 60 \qquad\qquad\qquad\qquad\text{(A3)}$$

928   and

929        $$t_{HP,E}(i) = t_O + (i+1) \cdot 60. \qquad\qquad\qquad\qquad\text{(A4)}$$

930   In Eqs. A3-A4 the index is $i \in \{0, 1\}$. A special case with $i = 2$ is also analyzed in Sect. 3.5,

931   Analogous to the recursion in Eq. A4, the ending time of a WCR averaging interval is

932        $$t_{WCR,E}(i) = t_O - i \cdot 60 \cdot v_w / gs. \qquad\qquad\qquad\qquad\text{(A5)}$$

933   Here v_w is a wind advection speed (discussed below) and the second term on the rhs is a wind

934   advection distance divided by the WKA (Wyoming King Air) ground speed (gs). Analogous to

935   the Eq. A5, the beginning time of a WCR averaging interval is

936        $$t_{WCR,B}(i) = t_{WCR,E} - (i+1) \cdot 60 \cdot v_w / gs \qquad\qquad\qquad\qquad\text{(A6)}$$

937   The wind advection speed (v_w) in Eqs. A5-A6 was calculated using an altitude-

938   dependent west-to-east wind velocity (u) and an altitude-dependent south-to-north wind

939   velocity (v). These altitude-dependent component velocities were calculated using the

940   horizontal wind vectors in the penultimate and last columns of Table 2. Plots of the component

941 velocities versus altitude and the linear functions used to relate component velocities to altitude

942 are presented in Figs. A1a-b.

943 An altitude ($z' = 3400$ m) was assumed for evaluating the horizontal wind advection

944 vector. This is the altitude of the ridges west and northwest of the HP site (Figs. 3a-b).

945 The WKA track vector (Table 2) defines the vertical plane of the WCR measurements.

946 We assumed that wind advection of snow particles occurred parallel to this vector. With the

947 assumption stated in the previous paragraph, the horizontal wind advection speed (v_w) was

948 calculated as the projection of the horizontal wind vector onto the track vector.

949
$$v_w = \frac{u(z') \cdot gs_x + v(z') \cdot gs_y}{\left(gs_x^2 + gs_y^2\right)^{1/2}} \tag{A7}$$

950 In Eq. A7 the west-to-east and south-to-north components of the track vector are symbolized gs_x

951 and gs_y. Vector representations of the track vector are in Table 2. On 14/15 December 2016 and

952 3 January 2017, the values of v_w are 7.4 and 8.9 m s^{-1}, respectively.

953 In addition to the properties gs and v_w used to evaluate Eqs. A5-A6, a WCR averaging

954 interval/domain was evaluated using a snow particle downward speed (Eq. A8).

955
$$v_p = |<V_D>| + \sigma_{V_D} \tag{A8}$$

956 Here, $<V_D>$ is the average of Doppler velocities within an averaging interval/domain, $|<V_D>|$

957 is the absolute value of the average, and σ_{V_D} is the standard deviation of the average. On both

958 the lhs and rhs of Eq. A8, all terms are greater than zero.

959 We interpret v_p as the maximum likely snow particle speed toward the ground. There are

960 three reasons for this: 1) For the WCR averaging intervals/domains we analyzed, values of

961    $<V_D>$ were consistently less than zero (Table 5). This indicates that snow particles (on average)

962   were moving toward the ground. 2) Again, for the WCR averaging intervals/domains we

963   analyzed, σ_{V_D} was comparable to $|<V_D>|$. This indicates that turbulent eddies transported snow

964   particles upward and downward at a speed comparable their downward speed in still air. 3) The

965   V_D are reflectivity weighted (Haimov and Rodi 2013) and are thus indicative of the motion of

966   the largest particles within an averaging interval/domain.

967   We now focus on the top boundary of a WCR averaging interval/domain. Figures 6b and

968   6d have representations of the boundary. The slope defining this boundary was calculated as

969    $-v_p \cdot gs / v_w$. That is, particles below this boundary moved downward sufficiently fast and

970   horizontally sufficiently slow to advect reasonably close to the hotplate. Starting with diagnosed

971   values of gs and v_w, the values of v_p and slope, were derived iteratively. The precision of the

972   derived v_p is ± 0.1 m s^{-1}.

973

974
975
976
977
978
979
980
981
982
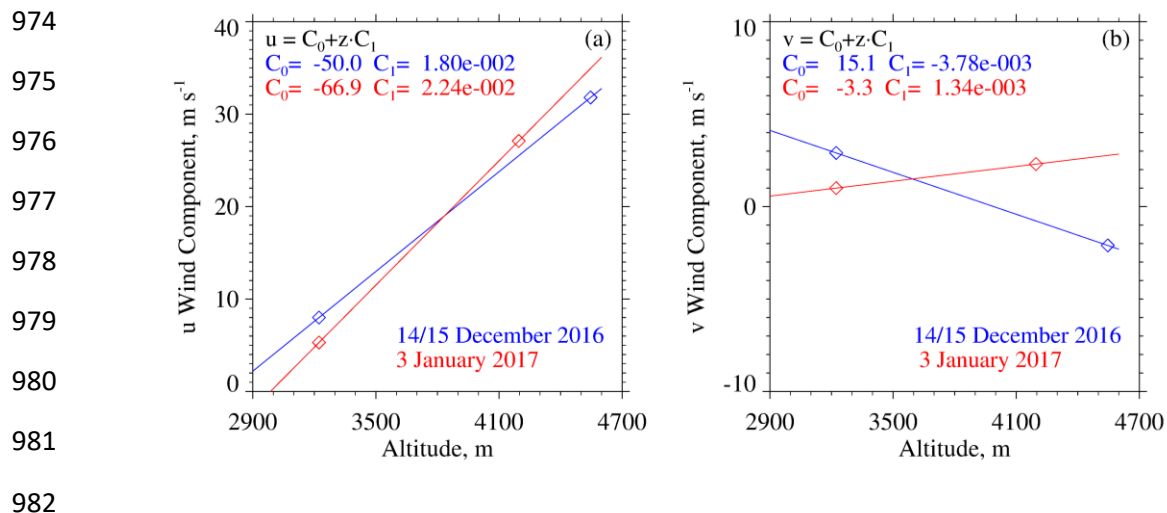
983   Figure A1 – (a) West-to-east (u) wind velocity derived using measurements from the WKA and

984   the AmeriFlux (AF) tower. Also shown is the linear function used to relate u to altitude. (b)

985   South-to-north (v) wind velocity derived using measurements from the WKA and AF. Also

986   shown is the linear function used to relate v to altitude. WKA and AF velocities are presented as

987   vectors in the penultimate and last columns of Table 2.

988

989   Data Availability. The WKA and WCR measurements can be obtained from the SNOWIE data

990   archive of NCAR/EOL, which is sponsored by the National Science Foundation. Hotplate gauge

991   measurements are at https://doi.org/10.15786/20103146. The US-GLE AmeriFlux measurements

992   are at https://ameriflux.lbl.gov/. The Brooklyn Lake SNOTEL gauge measurements are at

993   https://www.wcc.nrcs.usda.gov/snow/. Merged Hotplate, SNOTEL, and AmeriFlux data

994   sequences from 14/15 December 2016 and 3 January 2017 are in Snider (2023).

995

996   Author contributions. JS and MB wrote the grant proposal that funded this research. Field

997   measurements were performed by SF, SM, SH, MB, and JS. SF wrote her MS dissertation, and

998   this was adapted for this paper by JS. KS processed the snow particle imagery. AM maintained

999   the measurement sites. All authors contributed to the editing of this paper.

1000

1001 **Acknowledgements –**

1002   We acknowledge technical assistance provided by David Plummer, Larry Oolman, Zane

1003 Little, Brent Glover, Edward Sigel, Thomas Drew, and Brett Wadsworth. We thank SNOWIE

1004 project PI Jeffery French, who provided the flight data, Gabor Vali who provided the S/Z data

1005 points in Fig. 12a, and John Frank and John Korfmacher who acquired the GLE-US AmeriFlux

1006 data set. This work was supported by the United States National Science Foundation (Award

1007 Number 1850809) and the John P. Ellbogen Foundation.

1008

References

AmeriFlux, https://ameriflux.lbl.gov/, 2021

Battaglia, A. and Panegrossi, G., What Can We Learn from the CloudSat Radiometric Mode Observations of Snowfall over the Ice-Free Ocean?, 12, 3285, https://doi.org/10.3390/rs12203285, 2020

Boudala, F.S., R. Rasmussen, G.A. Isaac, and B. Scott, Performance of Hot Plate for Measuring Solid Precipitation in Complex Terrain during the 2010 Vancouver Winter Olympics, J. Atmos. Oceanic Technol., 31, 437–446, https://doi.org/10.1175/JTECH-D-12-00247.1, 2014

Braham , R. R., Snow Particle Size Spectra in Lake Effect Snows. J. Appl. Meteor. Climatol., 29, 200–207, https://doi.org/10.1175/1520-0450(1990)029<0200:SPSSIL>2.0.CO;2, 1990

Brock, F. V., and Richardson, S. J., Meteorological Measurement Systems, Oxford University Press, New York, 304 pp., 2001

Brown, P. R. A., and P. N. Francis, Improved Measurements of the Ice Water Content in Cirrus Using a Total-Water Probe. J. Atmos. Oceanic Technol., 12, 410–414, https://doi.org/10.1175/1520-0426(1995)012<0410:IMOTIW>2.0.CO;2., 1995

Cocks, S.B., S.M. Martinaitis, B. Kaney, J. Zhang, and K. Howard, MRMS QPE Performance during the 2013/14 Cool Season, J. Hydrometeor., 17, 791–810, https://doi.org/10.1175/JHM-D-15-0095.1, 2016

Faber, S., French, J. R., and Jackson, R., Laboratory and in-flight evaluation of measurement uncertainties from a commercial Cloud Droplet Probe (CDP), Atmos. Meas. Tech., 11, 3645–3659, https://doi.org/10.5194/amt-11-3645-2018, 2018

Falconi, M. T., von Lerber, A., Ori, D., Marzano, F. S., and Moisseev, D.: Snowfall retrieval at X, Ka and W bands: consistency of backscattering and microphysical properties using BAECC ground-based measurements, Atmos. Meas. Tech., 11, 3059–3079, https://doi.org/10.5194/amt-11-3059-2018, 2018

Field, P.R., Hogan, R.J., Brown, P.R.A., Illingworth, A.J., Choularton, T.W. and Cotton, R.J., Parametrization of ice-particle size distributions for mid-latitude stratiform cloud. Q.J.R. Meteorol. Soc., 131: 1997-2017. https://doi.org/10.1256/qj.04.134, 2005

Fuller, S.E., Improvement of the Snowfall / Reflectivity Relationship for W-band Radars, MS Thesis, Department of Atmospheric Science, University of Wyoming, 2020

1038 Geerts, B., Q. Miao, Y. Yang, R. Rasmussen, and D. Breed, An Airborne Profiling Radar Study of the
1039   Impact of Glaciogenic Cloud Seeding on Snowfall from Winter Orographic Clouds, J. Atmos. Sci.,
1040   67, 3286–3302, https://doi.org/10.1175/2010JAS3496.1, 2010

1041 Haimov, S., and Rodi, A., Fixed-Antenna Pointing-Angle Calibration of Airborne Doppler Cloud Radar,
1042   Journal of Atmospheric and Oceanic Technology, 30, 2320-2335, https://doi.org/10.1175/JTECH-
1043   D-12-00262.1, 2013

1044 Hiley, M. J., M. S. Kulie, and R. Bennartz, Uncertainty Analysis for CloudSat Snowfall Retrievals, J. Appl.
1045   Meteor. Climatol., 50, 399–418, 2011

1046 Kneifel, S., von Lerber, A., Tiira, J., Moisseev, D., Kollias, P., and Leinonen, J., Observed relations between
1047   snowfall microphysics and triple-frequency radar measurements. J. Geophys. Res. Atmos., 120,
1048   6034– 6055, doi: 10.1002/2015JD023156, 2015

1049 Kochendorfer, J., Nitu, R., Wolff, M., Mekis, E., Rasmussen, R., Baker, B., and Jachcik, A, Testing and
1050   development of transfer functions for weighing precipitation gauges in WMO-SPICE, Hydrology
1051   and Earth System Sciences, 2, 1437-1452, https://doi.org/10.5194/hess-22-1437-2018, 2018

1052 Korolev, A. V., E. F. Emery, J. W. Strapp, S. G. Cober, G. A. Isaac, M. Wasey, and D. Marcotte, Small ice
1053   particles in tropospheric clouds: Fact or artifact? Airborne Icing Instrumentation Evaluation
1054   Experiment, Bull. Amer. Meteor. Soc., 92, 967–973, https://doi.org/10.1175/2010BAMS3141.1,
1055   2011

1056 Kulie, M. S., and R. Bennartz, Utilizing Spaceborne Radars to Retrieve Dry Snowfall, J. Appl. Meteor.
1057   Climatol., 48, 2564–2580, https://doi.org/10.1175/2009JAMC2193.1, 2009

1058 Kulie, M. S., Milani, L., Wood, N. B., Tushaus, S. A., Bennartz, R., and L'Ecuyer, T. S., A Shallow
1059   Cumuliform Snowfall Census Using Spaceborne Radar, Journal of Hydrometeorology, 4, 1261-
1060   1279, https://doi.org/10.1175/JHM-D-15-0123.1, 2016

1061 Lawson, R. P., O'Connor, D., Zmarzly, P., Weaver, K., Baker, B., Mo, Q., and Jonsson, H., The 2D-S
1062   (Stereo) Probe: Design and Preliminary Tests of a New Airborne, High-Speed, High-Resolution
1063   Particle   Imaging   Probe,   J.   Atmos.   Ocean.   Tech.,   23,   1462–1477,
1064   https://doi.org/10.1175/JTECH1927.1, 2006

1065 Liebe, H.J., Manabe, T., and Hufford, G.A., Millimeter–wave attenuation and delay rates due fog/cloud
1066   conditions, IEEE Trans. Antenn. Propag., 37, 1617–1623, 1989

1067 Liu, C.-L., and A. J. Illingworth, Toward more accurate retrievals of ice water content from radar
1068   measurements of clouds, J. Appl. Meteor., 39, 1130–1146, 2000

1069 Locatelli, J.D. and Hobbs, P.V., Fall speed and masses of solid precipitation particles, J. Geophys. Res., 79,
1070   2185–2197, https://doi.org/10.1029/JC079i015p02185, 1974

1071 Macklin, W.C., The density and structure of ice formed by accretion, Q.J.R.Meteorol.Soc., 88: 30-50.
1072   doi:10.1002/qj.49708837504, https://doi.org/10.1002/qj.49708837504, 1962

1073 Marlow, S.A, J.M. Frank, M. Burkhart, B. Borkhuu, S.E. Fuller, and J.R. Snider, Snowfall Measurements
1074   at Wind-exposed and Sheltered Sites in the Rocky Mountains of Southeastern Wyoming, in
1075   revision for the Journal of Applied Meteorology and Climatology, http://www-
1076   das.uwyo.edu/~jsnider/manuscript_revision2.docx, 2023

1077 Martinaitis, S.M., S.B. Cocks, Y. Qi, B.T. Kaney, J. Zhang, and K. Howard, Understanding winter
1078   precipitation impacts on automated gauge observations within a real-rime system, J. Hydrometeor.,
1079   16, 2345-2363, https://doi.org/10.1175/JHM-D-15-0020.1, 2015

1080 Mason, S. L., Chiu, C. J., Hogan, R. J., Moisseev, D., and Kneifel, S., Retrievals of riming and snow density
1081   from vertically pointing Doppler radars, Journal of Geophysical Research: Atmospheres, 123,
1082   13,807– 13,834, https://doi.org/10.1029/2018JD028603, 2018

1083 Matrosov, S.Y., Modeling Backscatter Properties of Snowfall at Millimeter Wavelengths, J. Atmos. Sci.,
1084   64, 1727-1736, https://doi.org/10.1175/JAS3904.1, 2007

1085 Moisseev, D., von Lerber, A., and Tiira, J., Quantifying the effect of riming on snowfall using ground-
1086   based observations, J. Geophys. Res. Atmos., 122, 4019–4037, doi:10.1002/2016JD026272, 2017

1087 Nemarich, J., Wellman, R.J., and Lacombe, J., Backscatter and attenuation by falling snow and rain at 96,
1088   140, and 225 GHz, IEEE Trans. Geosci. Remote, 26, 319–329, 1988

1089 Panofsky, H.A. and Dutton, J.A., Atmospheric Turbulence, Wiley-Interscience, New York, 397 pp., 1984

1090 Pokharel, B. and G. Vali, Evaluation of Collocated Measurements of Radar Reflectivity and Particle Sizes
1091   in Ice Clouds, J. Appl. Meteor. Climatol., 50, 2104–2119, https://doi.org/10.1175/JAMC-D-
1092   1005010.1, 2011

1093 Rasmussen, R.M., J. Hallett, R. Purcell, S.D. Landolt, and J. Cole, The Hotplate precipitation gauge, J.
1094   Atmos. Oceanic Technol., 28, 148-164, https://doi.org/10.1175/2010JTECHA1375.1, 2011

1095 R.M. Young Company, Model 05103 Wind Monitor, 2001

1096   Skofronick-Jackson, G., and Coauthors, The Global Precipitation Measurement (GPM) Mission for
1097   science and society, Bull. Amer. Meteor. Soc., 98, 1679–1695, https://doi.org/10.1175/BAMS-D-
1098   15-00306.1, 2017

1099   Smith, P.L., Equivalent radar reflectivity factors for snow and ice particles, J. Climatol. Appl. Meteor., 23,
1100   1258–1260, https://doi.org/10.1175/1520-0450(1984)023<1258:ERRFFS>2.0.CO;2, 1984

1101   Snider, J.R., Supplemental dataset for Marlow et al. (2023), https://doi.org/10.15786/20247870, 2023

1102   Surussavadee, C., and D. H. Staelin, Millimeter-Wave Precipitation Retrievals and Observed-versus-
1103   Simulated Radiance Distributions: Sensitivity to Assumptions. J. Atmos. Sci., 64, 3808–3826,
1104   https://doi.org/10.1175/2006JAS2045.1, 2007

1105   Tessendorf, S. A., and Coauthors, A transformational approach to winter orographic weather modification
1106   research: The SNOWIE Project, Bulletin of the American Meteorological Society, 100, 71–92,
1107   https://doi.org/10.1175/BAMS-D-17-0152.1, 2019

1108   Ulaby, F.T., Moore, R.K., and Fung, K., Microwave Remote Sensing: Active and Passive, Vol. 1,
1109   Microwave Remote Sensing Fundamentals and Radiometry, ARTECH HOUSE Inc., Norwood,
1110   MA, p. 456., 1981

1111   Vali, G. and Haimov, S., Observed extinction by clouds at 95 GHz, IEEE Trans. Geosci. Remote, 39, 190–
1112   193, 2001

1113   von Lerber, A., D. Moisseev, L. F. Bliven, W. Petersen, A. Harri, and V. Chandrasekar: Microphysical
1114   Properties of Snow and Their Link to Ze–S Relations during BAECC 2014. J. Appl. Meteor.
1115   Climatol., 56, 1561–1582, https://doi.org/10.1175/JAMC-D-16-0379.1, 2017

1116   Wang, P.K., and W. Ji, Collision Efficiencies of Ice Crystals at Low–Intermediate Reynolds Numbers
1117   Colliding with Supercooled Cloud Droplets: A Numerical Study, Journal of the Atmospheric
1118   Sciences, 57, 1001-1009, https://doi.org/10.1175/1520-0469(2000)057<1001:CEOICA>2.0.CO;2,
1119   2000

1120   Wilson, J., and E. Brandes, Radar measurement of rainfall—A summary, Bull. Amer. Meteor. Soc., 60,
1121   1048–1058, https://doi.org/10.1175/1520-0477(1979)060<1048:RMORS>2.0.CO;2, 1979

1122   Wolfe, J.P., and J.R. Snider, A relationship between reflectivity and snow rate for a high-altitude S-band
1123   radar, J. Appl. Meteor. Climatol., 51, 1111–1128, https://doi.org/10.1175/JAMC-D-11-0112.1,
1124   2012

1125   Zaremba, T.J., and Coauthors, Vertical motions in orographic cloud systems over the Payette River Basin.
1126   Part 1: Recovery of vertical motions and their uncertainty from airborne Doppler radial Velocity
1127   Measurements, in press at the Journal of Applied Meteorology and Climatology,
1128   https://doi.org/10.1175/JAMC-D-21-0228.1, 2022

1129   Zelasko, N., Wettlaufer, A., Borkhuu, B., Burkhart, M., Campbell, L. S., Steenburgh, W. J., and Snider,
1130   J.R., Hotplate precipitation gauge calibrations and field measurements, Atmos. Meas. Tech., 11,
1131   441-458, https://doi.org/10.5194/amt-11-441-2018, 2018

1132   Zikmunda, J. and Vali, G., Fall patterns and fall velocities of rimed ice crystals, J. Atmos. Sci., 29, 1334–
1133   1347, https://doi.org/10.1175/1520-0469(1972)029<1334:FPAFVO>2.0.CO;2, 1972

1134